oyal stronomical ociety

MNRAS **528**, 5377–5393 (2024) Advance Access publication 2024 February 5

SDSS-IV MaNGA: calibration of astrophysical line-widths in the $H\alpha$ region using HexPak observations

Sabyasachi Chattopadhyay,^{1★} Matthew A. Bershady ^⑤,^{1,2,3} David R. Law,⁴ Kyle Westfall,⁵ Shravan Shetty,^{2,6} Camilo Machuca,² Michele Cappellari ^⑥,⁷ Kate H. R. Rubin,^{8,9} Kevin Bundy⁵ and Samantha Penny ^⑥10

Accepted 2024 February 1. Received 2024 January 30; in original form 2023 December 29

ABSTRACT

We have re-observed \sim 40 low-inclination, star-forming galaxies from the MaNGA survey ($\sigma \sim 65~{\rm km\,s^{-1}}$) at \sim 6.5 times higher spectral resolution ($\sigma \sim 10~{\rm km\,s^{-1}}$) using the HexPak integral field unit on the WIYN 3.5-m telescope. The aim of these observations is to calibrate MaNGA's instrumental resolution and to characterize turbulence in the warm interstellar medium and ionized galactic outflows. Here we report the results for the H α region observations as they pertain to the calibration of MaNGA's spectral resolution. Remarkably, we find that the previously reported MaNGA line-spread-function (LSF) Gaussian width is systematically underestimated by only 1 per cent. The LSF increase modestly reduces the characteristic dispersion of H II regions-dominated spectra sampled at 1–2 kpc spatial scales from 23 to 20 km s⁻¹ in our sample, or a 25 per cent decrease in the random-motion kinetic energy. This commensurately lowers the dispersion zeropoint in the relation between line-width and star-formation rate surface-density in galaxies sampled on the same spatial scale. This modest zero-point shift does not appear to alter the power-law slope in the relation between line-width and star-formation rate surface-density. We also show that adopting a scheme whereby corrected line-widths are computed as the square root of the median of the difference in the squared measured line width and the squared LSF Gaussian avoids biases and allows for lower signal-to-noise data to be used reliably.

Key words: techniques: imaging spectroscopy – galaxies: ISM – galaxies: kinematics & dynamics.

1 INTRODUCTION

Spectroscopic determination of gas and stellar motions – kinematics – is a fundamental diagnostic of physical conditions in the interstellar medium (ISM) and stellar dynamics, respectively. In SDSS-IV (Blanton et al. 2017), the BOSS spectrographs (Smee et al. 2013) on the *Sloan* 2.5-m Telescope (Gunn et al. 2006) were retrofitted with a suite of positionable, multi-object integral field units (IFUs; Drory et al. 2015) to conduct a large spectroscopic survey of nearby galaxies: Mapping Nearby Galaxies at APO survey (MaNGA; Bundy et al. 2015; Law et al. 2015; Yan et al. 2016a, b; Wake et al. 2017). MaNGA's unsurpassed spectral coverage (360–1000 nm) and sample size (more than 10 000 galaxies) provide an unprecedented dataset for analysis of the spatial distribution and properties of stellar populations (e.g. Neumann et al. 2022; Sánchez et al. 2022) as well

as the physical conditions of the ionized gas (e.g. Belfiore et al. 2016; Mingozzi et al. 2020; Schaefer et al. 2020) in galaxies over several decades in mass. However, the BOSS spectrographs with the MaNGA fibres are limited to a spectral resolution of $\sim\!2000$ equivalent to $\sim\!70$ km s $^{-1}$ (σ), several times larger than the intrinsic line-widths of gas and stars in normal, star-forming spiral discs and dwarf galaxies ($\sigma\sim10$ –20 km s $^{-1}$; e.g. Terlevich & Melnick 1981; Melnick, Terlevich & Moles 1988; Bender, Burstein & Faber 1992; Andersen et al. 2006; Epinat, Amram & Marcelin 2008; Martinsson et al. 2013; Penny et al. 2015). As a consequence of this instrumental limitation there has been relatively little exploration of disc stellar dynamics with MaNGA data, and in fact those studies that do have turned to proxies such as asymmetric drift (Shetty et al. 2020; Yang et al. 2021).

To circumvent these instrumental limitations on the MaNGA data application the MaNGA survey team have undertaken a major effort to characterize the BOSS spectrograph instrumental resolution (the line-spread function, or LSF; Law et al. 2016, 2021a) as part of the

¹South African Astronomical Observatory, 1 Observatory Rd, Observatory, 7925 Cape Town, South Africa

²University of Wisconsin, Department of Astronomy, 475 North Charter Street, Madison, WI 53706, USA

³Department of Astronomy, University of Cape Town, Private Bag X3, 7701 Rondebosch, South Africa

⁴Space Telescope Science Institute, 3700 San Martin Drive, Baltimore, MD 21218, USA

⁵University of California Observatories, University of California, Santa Cruz, 1156 High St., Santa Cruz, CA 95064, USA

⁶Kavli Institute for Astronomy and Astrophysics, Peking University, 100871 Beijing, China

Sub-department of Astrophysics, Department of Physics, University of Oxford, Denys Wilkinson Building, Keble Road, Oxford OX1 3RH, UK

⁸Department of Astronomy, San Diego State University, San Diego, CA 92182 USA

Ocenter for Astrophysics and Space Sciences, University of California, San Diego, La Jolla, CA 92093, USA

¹⁰Institute of Cosmology & Gravitation, University of Portsmouth, Dennis Sciama Building, Portsmouth, PO1 3FX, UK

^{*} E-mail: sabyasachi@saao.ac.za

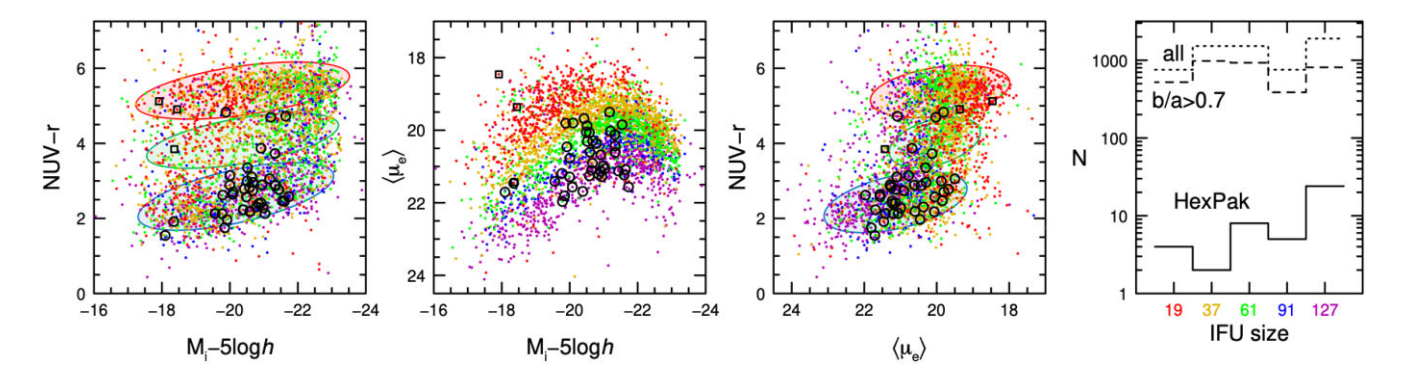


Figure 1. Distribution of HexPak targets (black open symbols, see text) in NUV-r rest-frame colour, *i*-band absolute magnitude (*AB* mag), and mean *i*-band surface-brightness (*AB* mag arcsec⁻²) within the elliptical half-light radius (see Table A1) overlaid on the parent MaNGA MPL-8 sample for 3628 galaxies with b/a>0.7. The parent sample is coloured by IFU size (fibre count), coded in the right-hand histogram. Red, blue, and green ellipses in the first and third panels mark the approximate respective locations of the red galaxy sequence, the star-forming main sequence (or blue cloud), and a transition region (i.e. the green valley).

deliverable science products provided by MaNGA's Data Analysis Pipeline (Belfiore et al. 2019; Westfall et al. 2019). The quality of this characterization is of such high fidelity that current estimates of the LSF provide corrections approaching what is required to achieve reliable line-widths at the $\sigma \sim \! 20 \text{--}30~\text{km}\,\text{s}^{-1}$ level for individual emission lines. The effort promptly yielded two significant scientific results on the nature of the ionized gas in galaxies concerning the correlation of (i) line-ratios and line-widths (Law et al. 2021b) that separates H II-like from diffused ionized gas; and (ii) line-widths to star-formation rate (Law et al. 2022) that provides a definitive local calibration of star-formation feedback-driven turbulence.

However, the MaNGA LSF calibration hinges on direct comparison with a reference set of a relatively small number of observations at higher spectral resolution. The largest high-resolution comparison is the DiskMass Survey (Bershady et al. 2010a, b; Westfall, Bershady & Verheijen 2011; Martinsson et al. 2013; Westfall et al. 2014), which provides line-widths for H α nebular emission as well for integrated star-light. However, the overlap of DiskMass and MaNGA is only seven galaxies. The DiskMass Survey H α spectra have $R \equiv \lambda/\delta\lambda \sim$ $10\,000\,(\sigma \sim 9.9\,\mathrm{km\,s^{-1}})$. Given the importance of understanding the fidelity of these corrections for a wide range of science applications, we have undertaken a new calibration of the MaNGA LSF by reobserving 43 galaxies from the MaNGA sample in H α at even higher spectral resolution with a different spectrograph, IFU, and telescope. These new, high-resolution data were taken not only for purposes of calibrating the MaNGA LSF, but also to determine the impact of the MaNGA LSF on detecting galactic winds. The latter will be reported in a separate publication (Chattopadhyay et al., in preparation).

This paper is organized as follows. Section 2 presents the sample selection and describes the new data acquired with the HexPak IFU at the WIYN 3.5-m telescope along with the basic image processing and spectral extraction. Section 3 details measurements of the WIYN Bench Spectrograph LSF using two different tracers, and the spatial registration of MaNGA and HexPak IFUs. In Section 4 we compare the HexPak and MaNGA H α line-widths, corrected for instrumental broadening. We use the systematic differences between these linewidths to derive a correction to the MaNGA LSF estimate. Section 5 provides illustrations of the scientific impact of this correction to the MaNGA LSF. In Section 6 we summarize our conclusions from these sections in the context of the H II-like line-width distribution and the correlation between H α line-width and star-formation surface-density. Throughout, we follow the nomenclature from Law et al. (2021a) where σ refers to the observed or corrected Gaussian line-

width of an astrophysical source, while ω refers to the Gaussian profile characterization of the spectrograph LSF as measured from the widths of monochromatic arc or sky lines. Line wavelengths are specified in air.

2 DATA

2.1 Sample selection from MaNGA

We targeted low-inclination galaxies with axis ratios b/a>0.7 from galaxies observed by and included in the MaNGA Project Launch-8 (MPL-8), released internally in 2018 November. This parent sample consists of datacubes for 6430 galaxies, post-dates the public Data Release (DR)-15 (Aguado et al. 2019) and predates DR-17 (Abdurro'uf et al. 2022), but is fully contained in the latter. Low-inclination galaxies were selected to minimize line-of-sight effects and to be sensitive to winds. We also inspected all relevant datacubes to ensure that they had reasonable kinematic signal in ionized gas (moderate to high star-formation) and integrated starlight (continuum surface-brightness above 22 mag arcsec⁻² within the half-light radius in the i band).

Due to instrument constraints on spectral coverage at high resolution, source redshifts between 0.018 < z < 0.028 were required to ensure [S II] $\lambda\lambda$ 671.7, 673.0 nm was captured in the echelle, order 8 setup for the H α region (this set the upper redshift limit), while [O III] λ 500.7 nm was captured in the VPHg setup for the Mgb region (this set the lower redshift limit).

All considerations being equal, we preferentially observed targets with HexPak that had been observed in the larger MaNGA IFUs. This was for the practical reason that the HexPak IFU has a larger footprint that the MaNGA IFUs, while the inner 4 arcsec (radius) of the MaNGA data has significant beam-smearing (Law et al. 2021a); the larger MaNGA IFUs therefore provide the greatest spatial overlap where kinematics can be well compared. We note that this preferentially samples lower surface-brightness galaxies (Wake et al. 2017), as seen in Fig. 1 here. However, we do sample galaxies over a wide range of total star-formation from 0.05 to 3 $\rm M_{\odot}~yr^{-1}~(\it H_0=70~km~s^{-1}~Mpc^{-1})$.

A target table with salient data is given in Appendix A, Table A1. Fig. 1 shows the distribution of HexPak targets in rest-frame colour, luminosity, and surface-brightness within the larger MaNGA low-inclination sample (MPL-8; b/a<0.7). The distribution shows our preference for blue star-forming galaxies observed with larger

MaNGA IFU sizes, and within these constraints, with higher surface-brightness.

Finally, three low-mass AGN hosts, selected from Penny et al. (2018), were observed in the first semester of the programme: 1–230177, 1–379255, 1–38618. These are marked with open squares in Fig. 1. None of these targets exhibited strong $H\alpha$ emission in the HexPak data, and had very little radial extent. These galaxies have been excluded from the remaining analysis.

2.2 New observations: HexPak

The program was awarded 20 nights on the WIYN 3.5-m telescope¹ using the HexPak IFU (Wood et al. 2012) and the upgraded Bench Spectrograph (Bershady et al. 2008; Knezek et al. 2010) over three observing semester starting in the second half of 2018. HexPak is roughly a 41 by 36 arcsec hexagon of 84×2.81 arcsec diameter fibres with a 6 arcsec diameter core of 18×0.94 arcsec diameter fibres in three rings. HexPak is the first of two variable pitch IFU, feeding the Bench Spectrograph in a dual slit shared with the ∇ Pak IFU (Eigenbrot & Bershady 2018). Of the time awarded six nights had good conditions, seven nights had poor conditions, and seven nights were not usable at all. A total of 43 galaxies were observed in the H α spectral region, which are reported here.

These observations used the Bench Spectrograph configured for the R2 echelle (316 l/mm, blazed at 63.4°). The echelle is used 11.5 deg off-Littrow with a grating incidence angle $\alpha=65.4$ deg. In order 8, selected via an order-blocking interference filter (X19), the spectra are centreed at 675.7 nm and cover 654.9–694.3 nm on the STA1 2600 \times 4000 pixel CCD. This device has 12 μm pixels, but was used in a 2 \times 2 binning mode to reduce read-noise. In this mode the system delivers 4.1 e- rms read-noise per 24 μm super-pixel.

The Bench Spectrograph has a geometric demagnification factor of 0.356; with the echelle configuration, there is an additional anamorphic factor of 0.723 in the spectral dimension. Adopting the effective full width at half-maximum (FWHM) slit-width of a round aperture of diameter D as $\cos(30) \times D$, we expect the monochromatic image of the larger (smaller) fibres to be 2.8 (0.9) super-pixels in the absence of significant aberrations. With the delivered linear dispersion from the echelle of 0.019 nm per super-pixel, we anticipate a spectral resolution $R = \lambda/\delta\lambda \sim 12850$ for the large fibres and, in the absence of optical aberrations, three times higher for the smaller fibres. However, the latter are significantly under-sampled, and they only yield ~ 50 per cent higher spectral resolution than the larger fibres due to aberrations. Since accurate knowledge of the instrumental resolution is very much of the essence for this analysis, the delivered resolution is measured in Section 3.

Typical $H\alpha$ spectroscopic observations consisted of a total of 1 h of integration split between three, 20-min exposures for cosmic-ray removal. There was no dithering between frames so that the nominal field coverage retains the interstitial fibre gaps. For our purposes of mapping to the MaNGA data with complete coverage this sampling was adequate. The rotator on the WIYN Instrument Adaptor System was always positioned to keep HexPak oriented in the same manner as the MaNGA IFU observations.

Calibration data consists of bias, dark, dome-flat, and thorium-argon arc-lamp exposures. There is significant bias and dark structure in STA1; 50–100 frames of each were taken over the course of a run

and combined to minimize contributed noise in the standard object frame reduction process. Dome-flats and arc-lamp frames were taken at several exposures to provide adequate counts in the small fibres yet avoid saturation in the large fibres. It is worth noting in what follows below that the arc-lamp light injection into the fibres does not follow the same light path as the dome-flats or sky, and as a consequence likely illuminates the fibres with a different *f*-ratio.

Additional observations of seven galaxies in the H α sample were made in the second and third semesters in a second, medium resolution configuration sampling from [O III] λ 500.7 nm through to the Mg I triplet near 517 nm. These data and results therefrom are reported in a later paper. Here we specify the configuration as it has bearing on our sample selection. A 3300 l/mm volume-phase holographic grating was used in a first order Littrow configuration with grating angle close to 59.5°; no blocking filter was required. This configuration provides a central wavelength of 522.2 nm and coverage between 508.4 and 534.2 nm. Spectral resolution was \sim 20 per cent lower than the echelle observations in the H α region.

Standard IRAF² tools designed for image processing (ccdred package) and the Bench Spectrograph spectral extraction (HYDRA package) were adapted and used. The only significant augmentations were for (i) handling the two fibre sizes in the HexPak array, similar to what is discussed by Eigenbrot & Bershady (2018) for dealing with the five fibre sizes in ∇Pak , and (ii) for sky-subtraction, as discussed below.

2.2.1 Sky subtraction

HexPak has seven large and two small sky fibres. We implemented a custom IRAF routine for independent sky subtraction of large and small HexPak object fibres using these sky fibres based on concepts illustrated in Bershady et al. (2005). This subtraction operates on wavelength-calibrated, field-flattened, and rectified spectra; in IRAF these are referred to as 'ms' files, while in MaNGA they are referred to as 'row-stacked spectra.' The data format arranges the spectra in order as they appear in the fibre pseudo-slit, with every wavelength channel aligned in one data index.

The subtraction routine begins by fitting a polynomial to the continuum of every fibre (including sky fibres) and subtracting it out. The continuum-subtracted spectra are used for source emission line analysis. The continuum fitting uses a $\pm 3\sigma$ clipping to remove source and sky emission lines and any remaining detector artefacts from the estimate of the continuum. In the case of the echelle data a third-order Legendre polynomial was adequate to represent the continuum. The continuum spectral fits are saved for spatial registration purposes (Section 3.3), which for this purpose have the mean sky-fibre continuum spectra (large and small, separately) subtracted.

Given the few small sky-fibres, the two continuum-subtracted sky spectra were simply averaged and then subtracted from the small object fibres, leaving the final, continuum- and sky-line subtracted spectra for final emission-line analysis. The large sky fibres trace uniformly (but sparsely) along the full pseudo-slit. These were fit separately in each wavelength channel with a low order function. The function is then interpolated along the pseudo-slit and subtracted from the object fibres for final emission-line analysis. The purpose

¹The WIYN Observatory is a joint facility of the University of Wisconsin—Madison, Indiana University, NSF's NOIRLab, the Pennsylvania State University, Purdue University, and the University of California, Irvine.

²IRAF was distributed by the National Optical Astronomy Observatory, which was managed by the Association of Universities for Research in Astronomy (AURA) under a cooperative agreement with the National Science Foundation.

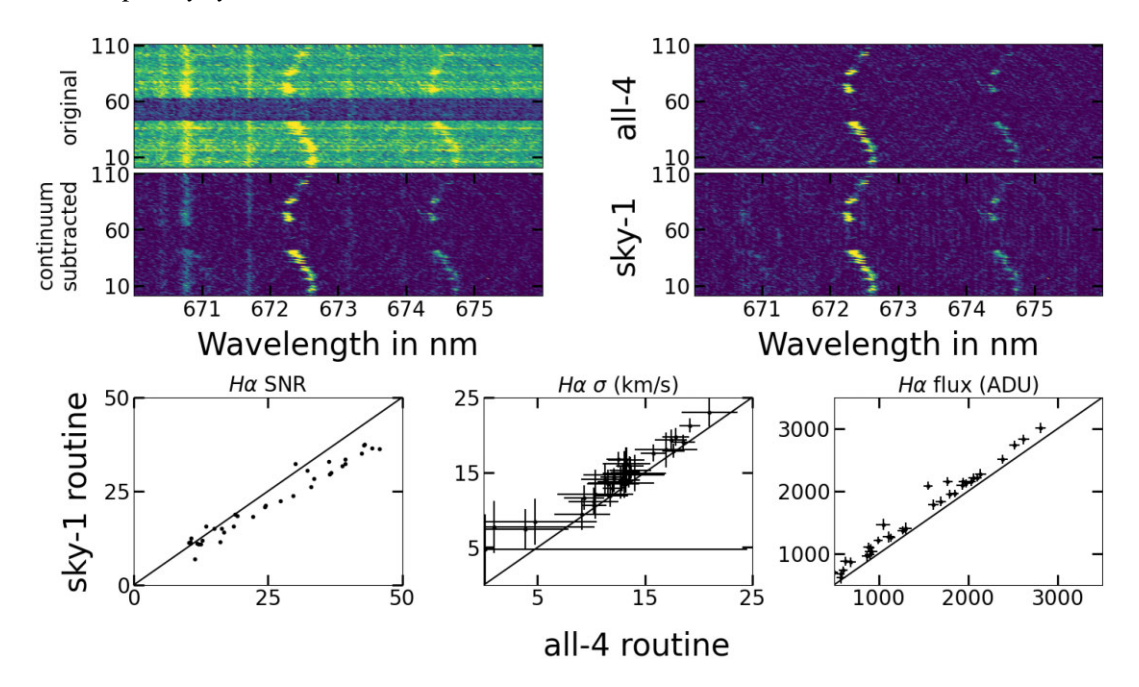


Figure 2. Effects of sky-subtraction procedure on the measured SNR, line flux and line widths for galaxy 1–37018 in the Hα + [N II] region. The left top panel shows the reduced, wavelength calibrated, telluric-corrected, normalized spectra, while the left middle panel shows the same after continuum subtraction. Right top and middle panels show the continuum-subtracted spectra after sky subtraction through all-4 and sky-1 routines respectively. The HexPak fibre ID is on the *y*-axis. The bottom three panels, left to right, compares SNR, line-width (km s⁻¹) and line-flux (instrumental units) measured for fibres with Hα SNR > 10 in the Hα line emission measured from the all-4 sky-subtracted spectra (*x*-axis) and the sky-1 sky-subtracted spectra (*y*-axis).

of a non-constant function is to model the variation in the sky-line profiles due to changes in aberrations and sampling along the fibre pseudo-slit. Higher-order functions (order 3–5) are desirable but are not well constrained with the small number of sky fibres. In the end, we reduced to order 1 (a constant, essentially the same as a clipped mean) to minimize residual structure in the line-free regions; order 3 minimizes residuals in bright lines, but adds substantially more structure in line-free regions. The line-subtraction is robust but still adds visually detectable coherent noise to the 2D spectra since only seven fibres are being used to determine the sky-line level. The coherent noise is at a low level, and it is incoherent with respect to the source line-emission that is significantly doppler-shifted from fibre to fibre. Hereafter we refer to this as the 'sky-1' routine.

Because the data is at such high dispersion, most of the fibre channels at any given wavelength are free from source line-emission even at wavelengths where, e.g. $H\alpha$ and other nebular lines are present. This offers the potential opportunity to reduce the noise introduced in sky-line subtraction by using all of the large fibres, with sigma clipping, to determine the sky-line level which, in contrast will be nearly constant in all fibres. The small fibres are treated as before in the sky-1 routine. With more large fibres, we are able to fit and then subtract a fourth order polynomial with σ-clipping as before for the continuum, here to remove sky-line emission. We refer to this as the 'all-4' routine. Visually, the sky-subtraction appears to be vastly improved in terms of reducing coherent noise from spectral channel to channel, but some over-subtraction of source flux is apparent in some fibres despite attempts to optimize the σ -clipping. Since oversubtraction could systematically clip source emission-line wings, this is a concern. Therefore, we compared Gaussian fitting results (described below) between the two sky-subtraction routines. Fig. 2 illustrates, for \sim 37 fibres with signal-to-noise (SNR) > 10 for galaxy 1-37018, the difference between the all-4 and sky-1 routines. We find that the all-4 routine over-subtracts source-flux and under-estimates

line-width even though it improves SNR, albeit only at higher SNR where it is a less-useful gain. As a consequence, we adopted the sky-1 routine for our analysis.

3 MEASUREMENTS

For consistency with previous MaNGA analysis and best practice we adopt PPXF (Cappellari & Emsellem 2004; Cappellari 2017) to measure the emission-line centres, widths and fluxes of calibration arc lines, sky emission lines as well as galaxy nebular emission. In all cases we fit a single-component Gaussian line profile to each line. In the case of astrophysical nebular lines including $H\alpha$, [N II] $\lambda\lambda$ 654.8.658.4 nm, and [S II] $\lambda\lambda671.7.673.1$ nm we use the PPXF package with a single velocity and line-width for all lines, while allowing flux to vary, with the exception of the 3:1 ratio for the [NII] lines. However, for arc and sky emission lines, a modified version of the emission_line routine of ppxf_util.py is used for line wavelengths obtained from NOAO arc lamp catalogue within the observed wavelength range. Again using PPXF, we individually fitted Gaussian profile to extract instrumental dispersion to ~35 arc lines separately which sparsely sample the wavelength range with velocity constraints of $\pm 20 \text{ km s}^{-1}$.

3.1 Measurement of the Bench Spectrograph LSF from arc-lamps

Individual arc-lamp line wavelengths were fed into PPXF along with the arc-lamp spectra, given an initial velocity and line-width estimate. The PPXF widths, $\omega_{\rm arc}$, measured at the discrete arc-line wavelengths, are interpolated over wavelength using a fifth order Legendre polynomial. The polynomial degree reflects the shape of the focus curve for the Bench Spectrograph dioptric camera, which has a shape of a (sometimes tilted) 'Mexican hat.' This interpolation in $\omega_{\rm arc}$ is shown

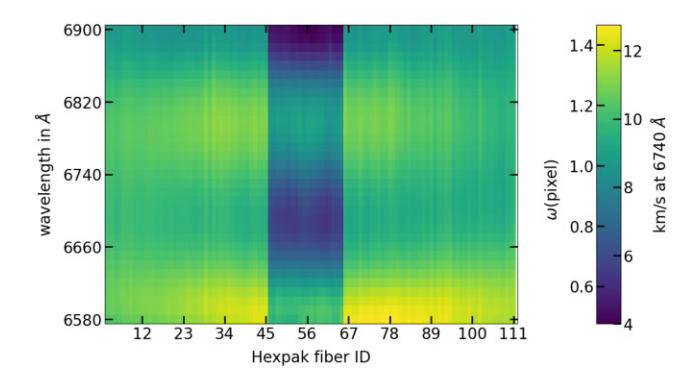


Figure 3. Distribution of arc line-widths (Gaussian width, ω , in pixels) across different HexPak fibres and the observed wavelength range of 658–690 nm. Arc-lamp line-widths, measured using PPXF are interpolated with a fifth-order Legendre polynomial in wavelength and rendered here at steps of 1 nm, i.e. at an interval of 20 pixels. The colour-bar is also referenced with the velocity equivalent of the arc line widths (σ) at the median wavelength of 674 nm. The fibres in the middle (fibre ID 45–65) with small instrumental line-widths are the 0.94 arcsec fibres.

in Fig. 3 in pixels and equivalent 1σ instrumental velocity resolution. Variations of instrumental line-width as a function of wavelength of this order (±20 per cent) are typical for the Bench Spectrograph. The characteristic instrumental resolution for the larger fibres is \sim 10 km s⁻¹, or R \sim 12,740, very close to our expectations from Section 2.2. We note that given our sampling is close to the critical value, the impact of the finite pixel size on our Gaussian width estimates should not be ignored (Robertson 2017; Law et al. 2021a). We use the default value pixel = True in the creation of the gas emission line templates in ppxf_util.emission_lines. By using PPXF to estimate these widths, in the parlance of Law et al. (2021a), we are measuring and reporting pre-pixelized estimates of the instrumental Gaussian line-width. Given our sampling this is likely to be about 3 per cent smaller than the post-pixelized values that would be estimated from simply fitting Gaussian functions evaluated at the pixel centres. The smaller fibres have characteristic instrumental resolution of ${\sim}6.5~\text{km}\,\text{s}^{-1},$ or $R{\sim}19\,600.$ These too are pre-pixeled Gaussian line-widths; their post-pixelized counterparts would be significantly larger. As an aside, we note the fact that the pre-pixelized LSF for the small fibres does not scale with the geometric size indicates that there are significant contributions from optical aberrations at the physical scale of the reimaged fibre FWHM of \sim 22 µm at the detector; we estimate the effective aberrations $\omega_{\rm abb} \sim 16 \mu {\rm m}$, again as a pre-pixelized value.

3.2 Measurement of the Bench Spectrograph LSF from sky lines

Sky-line widths are measured in the continuum-subtracted object spectra saved from the initial sky-subtraction stage described in Section 2.2.1, again individually for all fibres. There are 15 sky lines in the observed wavelength range out of which only 11 were fit with PPXF to derive $\omega_{\rm sky}$. These 11 lines were selected to ensure both arc and sky lines have wavelength overlap for fair comparison of $\omega_{\rm arc}$ to $\omega_{\rm sky}$.

We find, consistently, that for the large HexPak fibres the sky lines yield smaller instrumental line-widths ($\omega_{\rm sky} < \omega_{\rm arc}$), while the opposite holds for the smaller fibres ($\omega_{\rm sky} > \omega_{\rm arc}$). As demonstrated in figure 4, the differences are significant (e.g. the means and the error in the means of $\omega_{\rm arc}/\omega_{\rm sky}$ for large and small fibres are

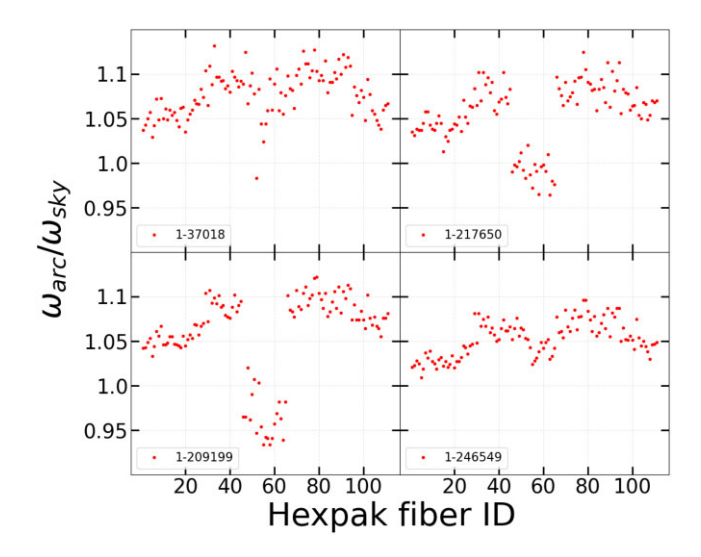


Figure 4. Ratio of HexPak instrumental width measured using LSF estimates from arc and sky lines ($\omega_{\rm arc}$ and $\omega_{\rm sky}$) at H\$\alpha\$ wavelengths. Panels show different galaxies observed on different nights and runs. Large and small fibres exhibit differences up to -6 per cent (small fibre) and + 12 per cent (large fibres). The outer large (2.8 arcsec) fibres tends to have smaller $\omega_{\rm arc}$ compared to central large fibres.

 1.08 ± 0.002 and 0.97 ± 0.006 respectively for the galaxy 1–209199), but because the instrumental line-widths are so small, the impact of these differences are very modest on corrected astrophysical linewidths that are likely for ionized gas. To illustrate this, we make the following simple calculation. Assuming Gaussian line profiles, we adopt the observed line-width $\sigma_{obs} = 22.4 \text{ km s}^{-1}$ so that the average corrected astrophysical line-width is $\sigma = 20 \text{ km s}^{-1}$. This value was chosen because it agrees with the mean value of our HexPak corrected measurements, as shown below. The uncertainty associated with this corrected line-width due to the variation between sky and arc LSFs is ± 0.3 km s⁻¹. Convolving this astrophysical linewidth and uncertainty with the nominal MaNGA LSF of 67.6 km s⁻¹ yields an observed line-width for MaNGA of 70.5 \pm 0.1 km s⁻¹. If this uncertainty were inferred as an uncertainty in the MaNGA LSF that would lead to commensurate MaNGA LSF uncertainty of only 0.14 per cent.

There is also a visible trend in the LSF differences between arc and sky lines for the large fibres within a galaxy. The large fibres closer to the slit centre demonstrate larger instrumental LSF differences compared to the edge fibres. This *might* be explained by the vignetting profile of the Bench Spectrograph: The redesigned collimator (Bershady et al. 2008; Knezek et al. 2010) is optimized for an f/5 injection beam, but sized for f/4 at the field edge (edge of the slit). Given the uncertainty of injection speed from the arc lamps, the arcs *may* have a faster output beam from the fibres than the sky. At the centre of the slit where there is the least vignetting, more of the light entering at larger angles (in a faster beam) will get through and lead to systematically larger aberrations, and hence larger arc line-widths compared to the sky lines. This model does not explain the different behaviour between the large and small fibres, but this shortfall does not impact our remaining analysis.

We performed the analysis in Section 4 after making a correction for the difference between ω_{arc} and ω_{sky} . As in Law et al. (2021a), because the sky-lines do not sample wavelengths as well as the arclines, the correction will be a suitable approximation. In the case of the HexPak echelle data, there are two clusters of sky lines, one at the red end and the other at the blue end of the wavelength range. The

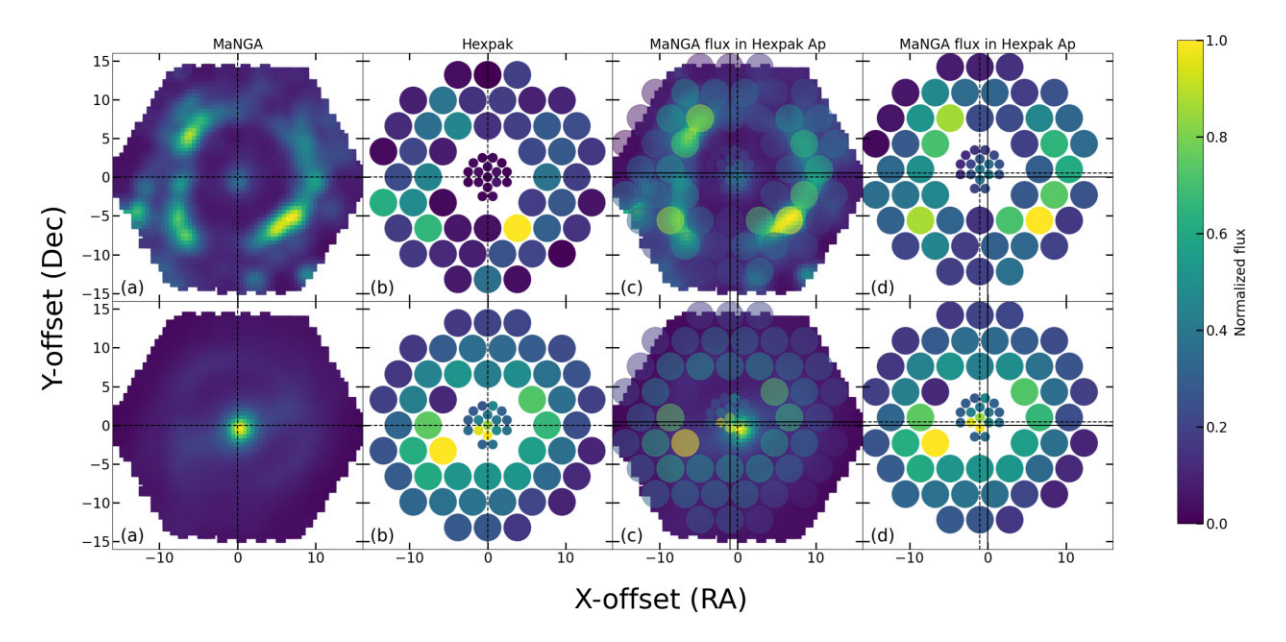


Figure 5. Typical X (RA) and Y (Dec) offsets between MaNGA and HexPak IFU pointings determined via cross-correlation of Hα line flux (top panels) and stellar continuum (bottom panels) for the galaxy 1–37211. Axes in each panel are sky-offsets in arcsec. Continuum offsets are (-0.4, 1.0) arcsec in (X, Y), and (-0.5, 1) for Hα. Panels from left to right shows (a) MaNGA measured flux, (b) HexPak measured flux, (c) MaNGA measured flux overlaid with MaNGA measured flux within the HexPak fibre footprint, and (d) MaNGA measured flux within the HexPak fibre footprint. The dashed horizontal and vertical lines in each panel represent field centres for the MaNGA datacubes (columns 1 and 3) and HexPak array (columns 2 and 4). Solid lines show the centre offset between HexPak and MaNGA (column 3) and MaNGA and HexPak (column 4) after registration.

bluer cluster of sky-lines shows a slightly larger offset in ω between sky and arc than the redder cluster of sky lines. We fit a linear function in wavelength to the difference $\omega_{arc} - \omega_{sky}$ to the full set of sky lines and apply this linear function to the Legendre polynomials shown in Fig. 3. As a consequence of making this correction we estimate any systematics in the corrected HexPak ionized gas linewidth introduce systematics in our estimate of the MaNGA LSF well below 0.1 per cent.

3.3 Spatial registration

We used a simple cross-correlation method to find the relative positions of the HexPak and MaNGA IFUs on the target galaxies, assuming no angular misalignment. Given the higher- resolution MaNGA data-cubes, this cross correlation sampled the MaNGA data-cubes given the HexPak fibre footprint in a process that is otherwise similar to what is described in (Bershady et al. 2005) for the SparsePak IFU. This process was done independently for the stellar continuum and the H α line-emission as shown in Fig. 5 to gauge the uncertainty in our estimates of the relative positioning between MaNGA and HexPak IFUs. For this example, the offsets are small and consistent between gas and star, as indicated by the dashed and solid horizontal and vertical lines in the figure. For the sample overall, as shown in Fig. 6, these two tracers yielded comparable results, with spatial offset measurements differing by <0.5 arcsec for about 70 per cent of the sample. In 35 out 40 galaxies the offset is within the large fibre footprint, and hence overall the offsets are small. The mean and standard deviation of the offset differences are 0.03 ± 0.67 arcsec and 0.07 ± 0.65 arcsec along X- and Y-directions, respectively. In terms of a radial offset differences between measurements from gas and stars, we find 90 per cent of the galaxies have difference < 0.5 arcsec, with mean and standard deviation of 0.08 \pm 0.34 arcsec. This indicates that the uncertainties in our spatial registration of the

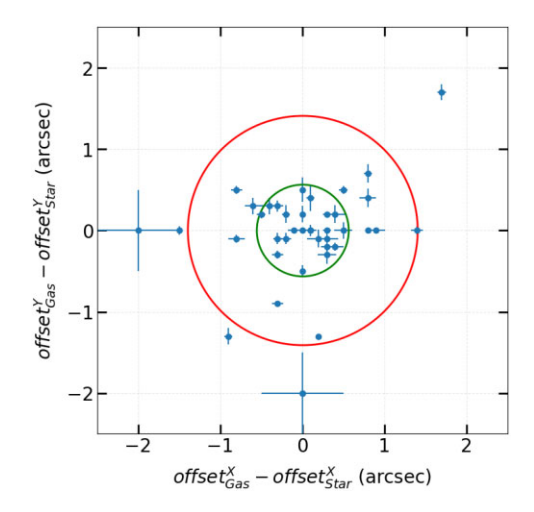


Figure 6. Differences between HexPak and MaNGA IFU spatial registration when estimated via cross-correlation of the H α flux distribution versus the stellar continuum distribution. Here X is RA and Y is Dec. Each point is a galaxy in our sample. The red and green circles represent footprints of the large and small fibres, respectively.

two IFU maps are well within their fibre footprints of 2.81 arcsec in diameter, and even the sub-sampled (0.5 arcsec) MaNGA datacubes.

4 ANALYSIS

4.1 Measurement biases in the corrected, Gaussian line-widths

In the presence of measurement error, two biases manifest in the estimation of Gaussian line-widths corrected for the effect of instrumental broadening: (i) positivity bias and (ii) survival bias. Positivity bias comes from fitting a function with positive-definite parameters to noisy data. In our case, this is a Gaussian function with a dispersion parameter $\sigma \geq 0$. The bias is not specific to the fitting routine (e.g. PPXF), but is a generic attribute of functional fitting with bounded parameters. As the uncertainty in the dispersion parameter estimate – due to errors in the data being fit – become comparable to, or greater in magnitude than, the actual line width, the distribution of the fitted dispersion parameters is biased, statistically, towards larger values than the underlying (actual) line width.

Survival bias comes from the numerical evaluation of the correction, in quadrature, of the measured dispersion parameter, σ_{obs} , and the instrumental line-width, ω , to estimate the astrophysical line-width, again: $\sigma=\sqrt{\sigma_{obs}^2-\omega^2}.$ In the presence of measurements errors on both σ_{obs} and ω , the argument of the square-root can be negative in some measurement instances; the chance of this happening increases (up to $\sim\!50$ per cent) as the combined measurement errors in σ_{obs} and ω become comparable to, or larger than σ , i.e. at low SNR and small σ/ω . In numerical analysis, imaginary values typically are censored from statistical computations, which in effect truncates the error distribution and systematically biases the distribution of estimated σ to larger values.

Both biases act to increase the corrected line-width above the intrinsic value, and these biases *increase* with *decreasing* SNR and, in the case of survial bias, with *lower* spectral resolution (*larger* ω). The effects of these biases in MaNGA data are well known: Westfall et al. (2019) discuss and simulate the 'positivity boundary bias' (what we call positivity bias here) in their Section 7.5.2, while Law et al. (2021a) simulate the impact of both biases in their Section 4.3. Both positivity and survival biases increase significantly the estimated MaNGA dispersion in the regime of the data evaluated in our study, well below the instrumental resolution. For similar reasons Law et al. (2021a, b) restrict their analysis of MaNGA gas line-widths to SNR > 50. Nonetheless, the corrections can become significant, and depend critically on the adopted functional form of the error distribution, as noted by both Westfall et al. (2019) and Law et al. (2021a), and as we discuss below.

In contrast, since the HexPak instrumental dispersion (the linewidth ω) is lower than the expected astrophysical dispersions, σ , in our data, we expect both the positivity and survival biases to be negligible for SNR \geq 10; see fig. 20 in Westfall et al. (2019) and fig. 15 in Law et al. (2021a), respectively. We restrict our consideration of HexPak line-widths to this SNR regime.

One way to ameliorate the impact of survival bias on MaNGA data³ is to work directly with the statistical distribution of σ^2 . As long as the mean or median of the *distribution* of σ^2 remains positive, the square-root of the mean or median becomes an unbiased estimator of σ . In general, the mean of the square-root is not equal to the square-root of the mean, so the median statistic is preferred. For this reason we propose the square-root of the median of the measurement distribution of $\sigma^2_{\rm obs} - \omega^2$ as an estimator of (the median) σ . In the following section we use new simulations to ascertain if this statistic is preferred over the corrected mean values described in Law et al. (2021a).

4.2 Simulations of positivity and survival bias in the corrected Gaussian line-widths

We evaluated the bias in recovered velocity dispersion as a function of intrinsic dispersion and SNR via a Monte Carlo simulation that used two different error distributions: a Gaussian function and an inverse gamma function (hereafter IGF). While the IGF may not be an immediately intuitive choice for the error distribution, in Bayesian statistics the error distribution of the width parameter for a Normal distribution, σ is indeed drawn from the IGF (e.g. Mackay 2003). Specifically, the probability density distribution of σ^2 is $P(\sigma^2) = \beta^{\alpha} \Gamma(\alpha)^{-1} \sigma^{-2(\alpha+1)} \exp(-\beta/\sigma^2)$ where α and β are related to attributes of the distribution and Γ is the gamma function. By fitting simulated Gaussian line profiles generated with random noise, it is straight forward to show that the measurement distribution appears to be well characterized by a Gaussian in the limit when the first moment of the distribution (e.g. the mean or mode of σ) is larger than the second moment (e.g. the square-root of the distribution variance); in this case the mean and mode are nearly equivalent. Indeed, this is the expected limiting behaviour of the IGF. However, when the second moment of the distribution is of order, or greater than the first moment, the distribution is asymmetric about the mode, which is also well represented by the IGF. In this limit the mean value of the distribution departs significantly from the mode, and the distribution is not well characterized by a Gaussian.

Unfortunately, there is some ambiguity in connecting the IGF functional parameters α and β to what might be observed in terms of unbiased estimators. For example, in the case of a Gaussian error distribution of the Gaussian line-width parameter σ , the distribution of the observed values of σ in the presence of measurement-error characterized by a variance ϵ^2 is expected to have a mean of σ and full-width half-maximum of 2.355ϵ . For the IGF, however, while the variance of the distribution can be associated with ϵ^2 , it is unclear if the IGF mode or mean (or some other statistic) is most appropriate to associate with σ . The two choices of mean or mode pose the easiest analytic forms for solving for the IGF parameters α and β ; from our simulations they appear likely to bracket a physical description relevant to the sampling parameters and astrophysical distributions of our data.

Hence here we consider these three different distributions that describe measurements in the presence of noise: (i) Gaussian; (ii) IGF with a mean formalism, where the distribution mean $\mu = \beta/(\alpha - 1)$; and (iii) IGF with a mode formalism, where the distribution mode $m = \beta/(\alpha + 1)$. The latter was adopted by Law et al. (2021a). Since the IGF can have significant skew, these choices impact the outcome of our simulations.

In our simulations we considered cases with SNR values of 10, 30, 50, and 100 as well all intrinsic dispersion values of $5 < \sigma_{true} < 45 \, \mathrm{km \, s^{-1}}$. For each combination of SNR and intrinsic dispersion, we computed the nominal dispersion (σ_{nom}) by convolving the intrinsic dispersion with nominal width of the LSF,

$$\sigma_{\text{nom}} = \sqrt{\sigma_{\text{true}}^2 + \omega_{\text{LSF}}^2}.$$
 (1)

In the context of the previous section we can equate $\sigma_{nom}=\sigma_{obs}$ and $\sigma_{true}=\sigma.$

For each SNR and σ_{true} we then created an observed distribution of 10^5 samples of σ_{nom} with a distribution width (ϵ) given by the relationship suitable for MaNGA data obtained from fig. 14 in Law et al. (2021a),

$$\epsilon = \sigma_{\text{nom}} \times 10^{-1.08 \times \log(\text{SNR}) + 0.24}.$$
 (2)

For the Gaussian error distribution the observed distribution of σ_{nom} has a mean equal to the nominal dispersion given in equation (1). For the IGF error distribution the value in equation (1) is equated either with the distribution mean (b) or mode (c).

³We thank M Blanton for pointing this out.

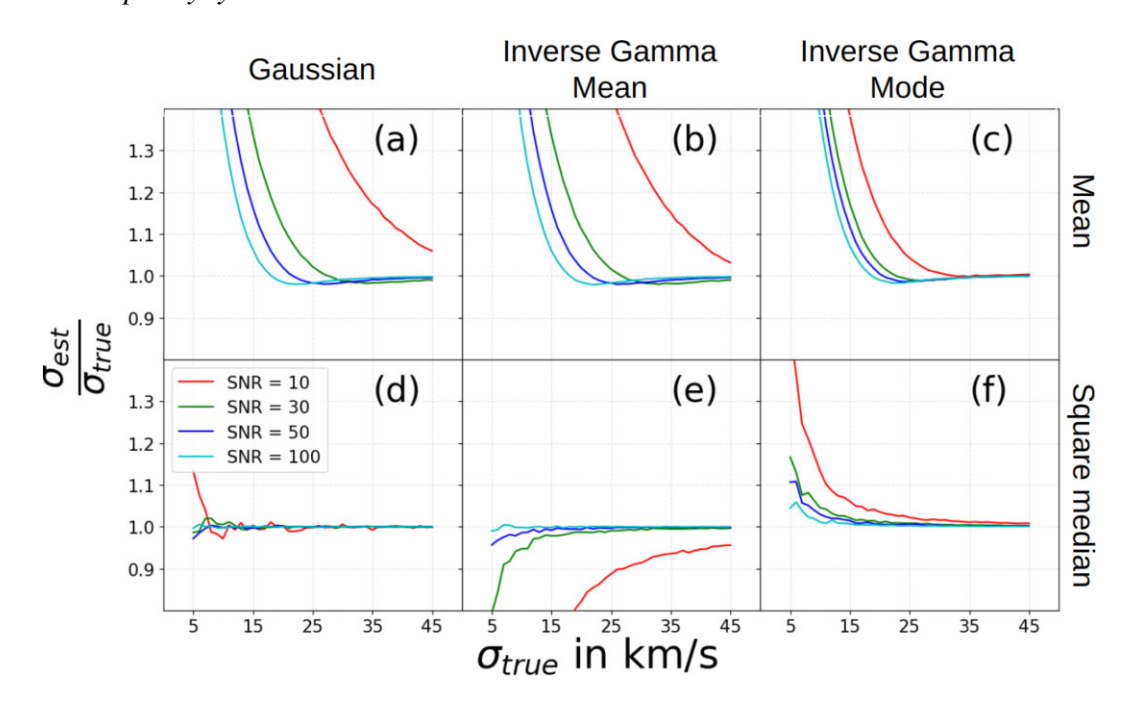


Figure 7. Simulations showing the percentage of bias in the recovered velocity dispersion for different SNR, different estimation methods, and different error distribution functions as a function of velocity dispersion. The ratio of recovered to model ('true') velocity dispersion is plotted against the model dispersion value. The top panels [(a), (b), c)] show the fractional bias introduced by mean estimation while the bottom panels [(d), (e), (f)] shows the same for square median estimation. Panels (a) and (d) show the performance adopt a Gaussian error distribution while the remaining panels adopt the IGF for the error distribution. The middle panels [(b) and (e)] and right panels [(c) and (f)] are computed with mean and mode formalization of the inverse gamma distribution.

Independently, we created an observed distribution of the LSF, ω , with the same number of samples as σ_{nom} . Following Law et al. (2021a), the distribution had a mean value of $\bar{\omega}=67.6~\text{km s}^{-1}$ and a Gaussian error distribution standard deviation, ϵ_{ω} , such that $\epsilon_{\omega}/\bar{\omega}=0.03$. These values well represent the expected distribution for the MaNGA LSF estimates. We then subtracted the square of each element in the LSF distribution (a randomized list) from the square of the corresponding element in the σ_{nom} distribution (an independently randomized list) to obtain the recovered dispersion distribution, σ_{est}^2 .

We examine the results of the simulations in Fig. 7 using two statistics of the σ_{est}^2 distribution. The first, shown in the top row, is the mean of the uncensored values of σ_{est} , i.e. the mean of the square-root of all values of $\sigma_{est}^2>0$. This estimator will contain survival bias; in the case of the IGF error distribution this estimator will also contain positivity bias. The top row is qualitatively similar to what is found in fig. 15 of Law et al. (2021a), as it should. The second statistic, shown in the bottom row, is the square-root of the median value of σ_{est}^2 . This is not expected to suffer from survival bias, but in the case of the IGF error distribution, should contain positivity bias.

Comparing the top and bottom rows in Fig. 7 it is evident that the median statistic has far less systematic bias at any given linewidth, SNR, and error distribution function. Indeed, for a Gaussian error distribution, the simulated biases are consistent with zero. With positivity bias, the square median estimation at SNR >=50 has ≤ 2 per cent bias in an astrophysically significant dispersion range, and even at SNR =10 the bias is only $\sim\!5$ per cent at $\sigma_{true}=15$ km s $^{-1}$ – a factor of 4.5 below the instrumental resolution.

Simulations such as these can be used to remove biases from linewidth measurements, as described for the mean estimator in Law et al. (2021a). However, bias removal requires good estimates of SNR as well as some ability to guess the intrinsic dispersion, i.e. σ_{true} . Law et al. (2021a) suggests that σ_{true} may be estimated by

using spaxels within a galaxy that have large SNR, usually 80 or higher. This approach could lead to biases or at least increase in random error in situations where, respectively (i) these spaxels do not well represent the intrinsic dispersion of the lower SNR spaxels being corrected, or (ii) the number of high SNR spaxels is small. The effect of error in the estimated intrinsic dispersion used to assign a correction to the mean and median statistics is shown in Fig. 8. Even for an extremely modest error in the estimated intrinsic dispersion (e.g. $\pm 1~{\rm km\,s^{-1}}$), the associated error in the corrected dispersion using the mean statistic becomes quite significant below 20 km s⁻¹ even at high SNR in MaNGA data. The corresponding error for the median statistic is much lower simply because the correction is much smaller.

These results re-enforce our proposal to use the median statistic based on the squared difference of the observed and instrumental dispersions. Here, and in the development that follows, we work with dispersions as squared values to avoid the issues of 'survival bias,' as described in Law et al. (2021a) and in Section 4.1 above; as we have shown in this section working directly with squared values is statistically robust and avoids the complication of modeling error distributions. Fig. 7 demonstrates that by adopting the median statistic of the squared difference of the observed and instrumental dispersions, a SNR threshold of 50 enables recovered dispersions to be within (+ 3, -2) per cent of the astrophysical dispersion at the expected thermal limit of $\sigma = 9 \text{ km s}^{-1}$, and roughly 5 per cent at the same limit for SNR = 30. At $\sigma = 18 \text{ km s}^{-1}$ systematics are < 1 per cent even at SNR = 30.

4.3 Application of the median estimator of line-width to MaNGA and HexPak data

In detail, at every spaxel, the MaNGA measured dispersion (σ_M) is corrected by the DAP-provided pre-pixelized LSF (ω_M) through

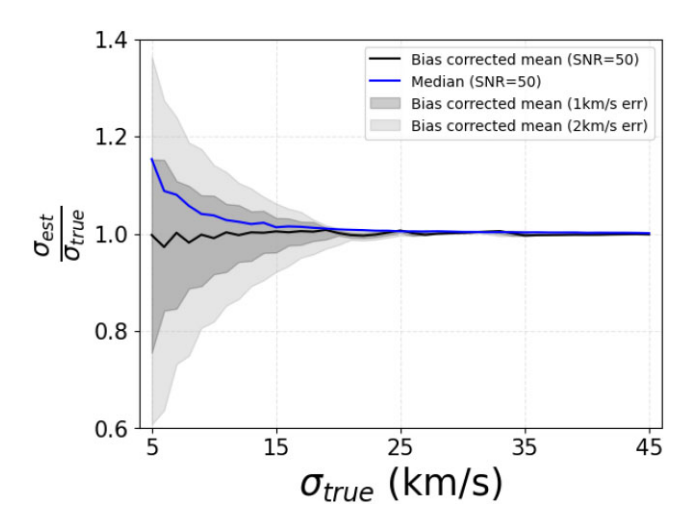


Figure 8. Effects of errors in estimating the intrinsic dispersion to compute the bias correction factor. The simulation is performed for the inverse gamma error distribution with the mode formalism. The solid black line represents the bias-corrected mean of the LSF-corrected dispersion, assuming no error in estimating the intrinsic dispersion, while the dark and light-grey shaded regions bound areas with limiting errors on estimating the intrinsic dispersion of 1 and 2 km s^{-1} , respectively, in computing the bias correction. The blue line is for the square-root of the median of the squared difference between the measured dispersion and the LSF [refer to Fig. 7(f)], for which there is no correction applied, and hence this measure does not depend on errors in the estimated intrinsic dispersion.

quadrature subtraction at the spaxel level,

$$(\sigma_{\mathbf{M}}^{\mathbf{c}})^2 = \sigma_{\mathbf{M}}^2 - \omega_{\mathbf{M}}^2,\tag{3}$$

assuming, as we do throughout, that the astrophysical and instrumental line-shapes are suitably approximated as Gaussians. Here σ_M is the pre-pixelized Gaussian velocity dispersion, derived from PPXF assuming no LSF, and ω_M is the pre-pixelized LSF Gaussian width – both as reported by the DAP. In principle we can compute a similar quantity at the fibre level for HexPak data.

In the present analysis we fit line profiles with a single-component Gaussian model which, in some cases, may be insufficient to parameterize the observed complexity in line-shape. Because we are restricting our analysis to data outside of the steep rise of the rotation curve, however, strongly asymmetric line-profiles due to beam-smearing are mostly absent. Further, we find that even for the high-resolution HexPak data the presence of weak, broadlined components (the topic of a future paper) do not significantly perturb the single component widths. I.e., in two-component fits the narrow-line component is nearly identical in width to that of a single component fit.

Before proceeding to apply the median estimators of $(\sigma_M^c)^2$ and $(\sigma_H^c)^2$, we investigated the SNR regime of MaNGA and HexPak data which may introduce survival bias. We did so in the specific context of the analysis here which compares the MaNGA spaxel measurements to HexPak fibre measurements. To make this a fair comparison we compare only spaxels within specific HexPak footprints to the HexPak values, but we include *all* of the MaNGA spaxels within the footprint regardless of the spaxel SNR.

As a practical matter, to proceed with our analysis we will limit our comparison to SNR thresholds in both the single-fibre HexPak data as well as the *median* SNR of MaNGA spaxels within HexPak footprints. In order to understand the implications of this decision on resulting MaNGA SNR distribution we compared the full MaNGA SNR distribution at the spaxel level to the median MaNGA SNR per footprint. Fig. 9 shows these distributions are nearly identical, but that the FWHM of the distribution of SNR values per HexPak footprint is comparable to the median value. This means that by imposing median SNR cuts we will be considering a broad range of MaNGA SNR.

With these SNR statistics in mind, we plot the median of $(\sigma_M^c)^2$ for all spaxels within each HexPak footprint, denoted $\langle (\sigma_M^c)^2 \rangle$, for HexPak footprints that have SNR > 10 within our sample in Fig. 10. This figures shows the distribution of the squared values of the HexPak LSF-corrected dispersions at SNR > 10 is always positive, while the median of the similar quantity for MaNGA spaxels within HexPak footprings do yield significant numbers of negative values. Hence for HexPak data with SNR > 10 there is no introduction of survival bias from correcting for the LSF broadening. Consequently, for HexPak we henceforth directly compute the LSF-corrected astrophysical dispersion σ_H^c by providing PPXF with a template which have sigma equal to the instrumental LSF, ω_H . However, $\langle (\sigma_M^c)^2 \rangle$ has negative data points at every MaNGA median SNR bin and hence survival bias would be significant had we considered a first-moment estimate (e.g. median) of the linear quantity σ_M^c .

We compare the LSF-corrected $H\alpha$ emission-line dispersions measured by MaNGA and HexPak in Fig. 11 for 4 galaxies in our sample. As depicted, the radial trends of LSF-corrected $H\alpha$ velocity dispersions are qualitatively similar for the two instruments, but for some galaxies the MaNGA measurements can be systematically higher or lower.

In Fig. 12 we plot the ratio of the MaNGA dispersion (σ_M^c) to the HexPak dispersions (σ_H^c), both LSF corrected, versus the corrected HexPak dispersions for the entire sample. Given the factor \sim 7 higher spectral resolution we adopt the HexPak measurements as a benchmark. If there were a consistent systematic error in the MaNGA LSF estimates we would expect to see a decreasing trend in the ratio toward larger line-widths, as indicated by the curves. In this figure we exclude all fibres within r<4 arcsec, to avoid beam-smearing issues. Fig. 12 shows the MaNGA dispersion values computed for three cases using the bias-corrected mean (with the three error distributions described in the previous section) and a fourth case using the median; in all cases the statistics are taken for the set of spaxels within each HexPak fibre footprint, using only footprints where the HexPak SNR > 10 and the median MaNGA SNR > 50. To estimate the mean bias correction factor in the first three cases, we used the mean LSF-corrected dispersion of MaNGA spaxels with SNR > 80 for each galaxy.

While the ratio of LSF-corrected dispersion values for individual fibres has considerable dispersion, the mean values show a clear positive offset consistent with an overall net bias in the MaNGA LSF estimate, which the balance of our analysis will quantify. Further,

scamble the input signal, and the MaNGA spaxels are constructed from a modified Shephard's algorithm that includes contributions from dithered fibre measurements within a radius up to 1.6 arcsec (Law et al. 2016). Hence the beam smearing in individual MaNGA spaxels measurements are already similar to that of a HexPak fibre. We do not take this approach in order to directly compare with and calibrate extant data from the DAP in the public domain.

⁴An alternative approach would be to coadd the MaNGA spectra and refit the line-width. While this might more closely replicate the HexPak beam-smearing, in practice the MaNGA and HexPak fibre footprints are very similar (1 and 1.5 arcsec fibre radii, respectively), fibres azimuthally

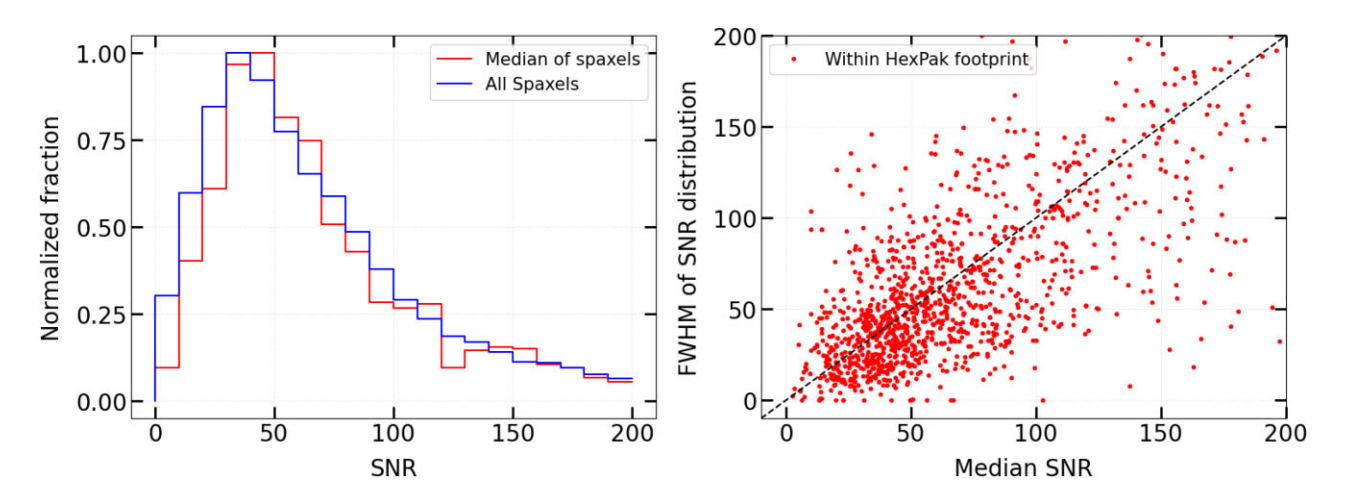


Figure 9. SNR distributions of MaNGA spaxels within HexPak footprints at radii between 4 and 15 arcsec and HexPak SNR > 10. Left: Histogram of all spaxels (blue) and the median (per footprint) of the same spaxels (red). Right: FWHM versus median of MaNGA SNR distribution within each HexPak footprint.

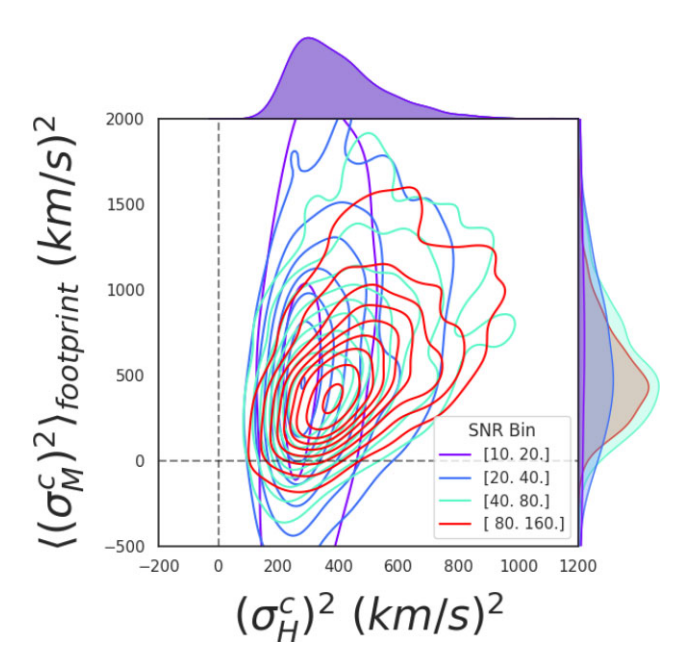


Figure 10. Distribution contours of LSF-corrected $H\alpha$ dispersions for the median MaNGA value for spaxels within HexPak footprints versus HexPak where the HexPak fibres have SNR > 10. Contour colours represent logarithmically increasing SNR intervals as defined in the key. Marginal histograms have identical SNR intervals.

while the results for the three bias-corrected mean prescriptions are very similar, the median prescription (which does not require a correction) marginally shows the best indication of a trend in the ratio with HexPak dispersion.

4.4 Systematic errors in the MaNGA instrumental line-width

We define the systematic error in ω_{M} as ω_{M}^{sys} such that

$$\left(\omega_{\mathbf{M}}^{\mathbf{c}}\right)^{2} = \omega_{\mathbf{M}}^{2} + \left(\omega_{\mathbf{M}}^{\mathbf{sys}}\right)^{2},\tag{4}$$

where ω_M^c is the systematic-corrected MaNGA LSF, and in principal $(\omega_M^{sys})^2$ can be either positive or negative. If we assume σ_H^c is much closer to the astrophysical dispersion than σ_M^c , we can expect that

$$\left(\sigma_{\rm H}^{\rm c}\right)^2 \sim \sigma_{\rm M}^2 - \left(\omega_{\rm M}^{\rm c}\right)^2. \tag{5}$$

Consistent with this assumption, Fig. 4 shows that the effect of any variation in measured ω_H is ≤ 10 per cent level to $(\sigma_H^c)^2$. This is due to the fact that ω_H is expected to be lower than σ_H^c . In contrast, this is not the case for MaNGA where ω_M is larger than σ_M^c , and hence even a minor correction in ω_M leads to large change in σ_M^c .

Combining equations (3), (4), and (5), we find

$$\left(\omega_{\rm M}^{\rm sys}\right)^2 = \left(\sigma_{\rm M}^{\rm c}\right)^2 - \left(\sigma_{\rm H}^{\rm c}\right)^2. \tag{6}$$

Both σ_M^c and σ_H^c are measured, so we can easily compute $(\omega_M^{sys})^2$. In practice we use $((\sigma_M)^2)$ within a given HexPak fibre footprint to compute $(\omega_M^{sys})^2$. Fig. 11 shows $(\omega_M^{sys})^2$ against radial distance of the same subset of four MaNGA galaxies discussed earlier. Low signal-to-noise (SNR \leq 10) points are excluded in the plot. Measurements in the shaded regions are excluded from our computation of the median systematic corrections; the larger radial distance cut (r < 15 arcsec) is used to ensure spatial overlap with MaNGA data while the lower cut (r > 4 arcsec) ensures spaxels affected with beam smearing are excluded

We then compute the median of $(\omega_{\rm M}^{\rm sys})^2$ of all the HexPak footprints mapped within each galaxy, denoted as $\langle (\omega_{\rm M}^{\rm sys})^2 \rangle_{\rm galaxy}$. Fig. 13 shows these median values for each galaxy, with distribution histograms given in Fig. 14. The latter also shows the distribution of $(\omega_{\rm M}^{\rm sys})^2$ for all of the individual measurements from all galaxies together. For this, we computed $(\omega_{\rm M}^{\rm sys})^2$ from equation (6) using the median value of σ_M^c for MaNGA spaxels within a given HexPak footprint where the median MaNGA SNR in the footprint is greater than 50 and the HexPak SNR is greater than 10. The HexPak dispersion, σ_H^c , is then subtracted in quadrature; we refer to this difference as $(\omega_{\rm M}^{\rm sys})_{\rm ensemble}^2$. Although the distribution is somewhat broader for the ensemble, the median values of $\langle (\omega_M^{sys})^2 \rangle_{galaxy}$ and $(\omega_M^{sys})_{ensemble}^2$ are identical at 96 km²s⁻², corresponding to a linear value $\langle \omega_M^{sys} \rangle$ of 9.8 km s⁻¹. Additionally the $\langle (\omega_M^{sys})^2 \rangle_{galaxy}$ distribution has 67 per cent confidence limit (CL) of $\pm 195 \text{ km}^2 \text{s}^{-2}$, or 14.0 km s^{-1} in linear units. This aligns with the error-weighted average and standard deviation of $\langle \omega_{\rm M}^{\rm sys} \rangle_{\rm galaxy}$ from Fig. 13 which is 99 and 187 km²s⁻², or 9.9 and 13.7 km s⁻¹ in linear units, respectively. Although in linear units $\langle \omega_{\rm M}^{\rm sys} \rangle = 9.8$ km s⁻¹ is a large fraction of the MaNGA LSF, $\omega_{\rm M} = 67.6$ km s⁻¹, when added in quadrature this amounts to only 1 per cent increase in MaNGA median LSF estimate. This is a systematic error in the MaNGA estimated LSF in addition to statistical uncertainties which is discussed in the next section.

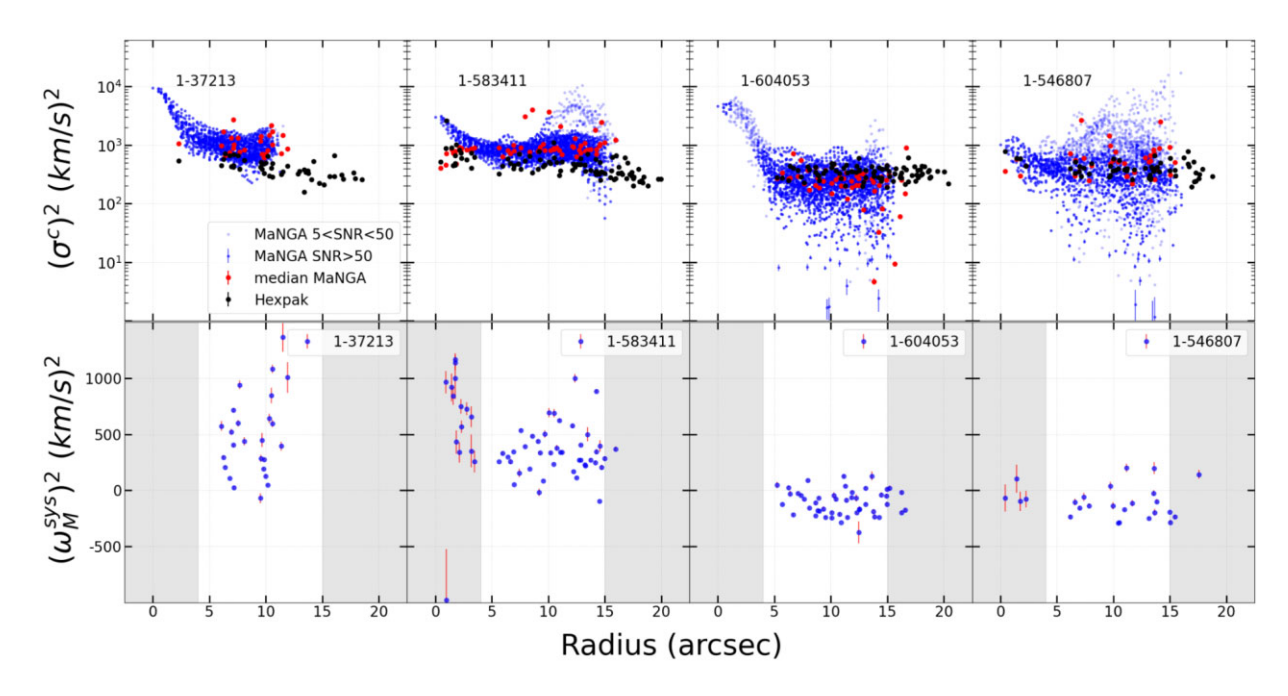


Figure 11. Radial distribution of LSF-corrected H α velocity dispersions (top row) and the square of the systematic error estimates of the MaNGA LSF (bottom row). In the top row individual MaNGA spaxels are shown as blue points, HexPak measurements from individual fibres with SNR > 10 are shown as black points, and median values for MaNGA spaxels in each of these HexPak fibre footprint where the median MaNGA SNR > 50 are shown as red points. Systematic error estimates, described in the text, are computed with equation (6). The MaNGA values of $(\sigma_M^c)^2$ used in this equation are a median of all the spaxels within the footprints of HexPak fibres. Data in the shaded regions (bottom row) are excluded from the median values, $((\omega_{NS}^{MS})^2)$, for individual galaxies.

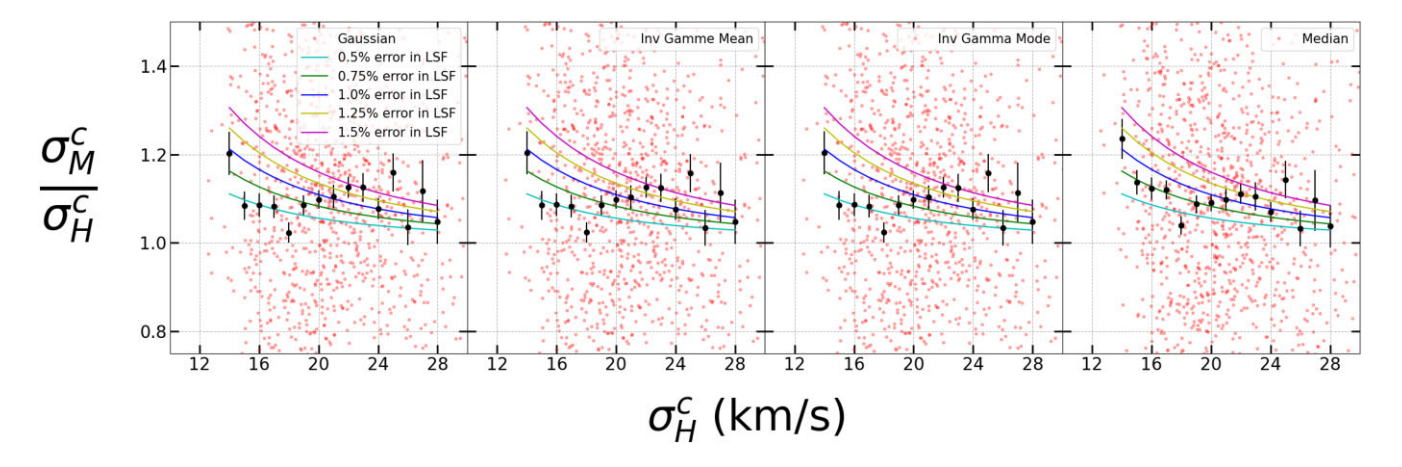


Figure 12. Ratio of LSF-corrected line-widths for MaNGA and HexPak versus the HexPak line-width. Red points represent ratios for individual HexPak fibre footprints with median MaNGA SNR > 50, as described in the text; the numerator is the median of the aggregate of *all* MaNGA spaxels in the footprint. Black data points represent the mean within a bin of 1 km s⁻¹ with error bars denoting the error in the mean. Panels (left to right) show ratios computed using bias-corrections adopting mean statistics for different error distributions, and the median. Curves indicate the expected relation with HexPak line-width assuming the MaNGA LSF is systematically *underestimated* by the labelled percentages.

5 IMPLICATIONS FOR ASTROPHYSICAL LINE-WIDTH DISTRIBUTIONS

5.1 Instrumental calibration

The conclusion from the analysis in the previous section is that the existing MaNGA spectral LSF as reported in Law et al. (2021a) and in DR-17 (Abdurro'uf et al. 2022) is too small by roughly 1 per cent, reckoned here at H α wavelengths: rather than a median LSF width of 67.6 km s⁻¹ at H α it should be 68.3 km s⁻¹. That this external calibration of the MaNGA LSF yields such a small change is a rather remarkable statement about the quality of the Data Reduction Pipeline (Law et al. 2016, 2021a). While a modest correction to the LSF, as we will show below, it does measurably

alter the line-width distribution for H II-like regions within MaNGA galaxies, particularly demonstrating a 25 per cent decrease in kinetic energy.

Further, from Figs 13 and 14, it appears that there is real variation between MaNGA data-cubes, with a 67 per cent confidence level of $\pm 14~\rm km~s^{-1}$ about $\langle \omega_M^{\rm sys}\rangle_{\rm galaxy}.$ This implies that while the calibration here should serve to accurately estimate astrophysical velocity dispersions from MaNGA data in the mean, the measured distribution of these widths will be broadened by roughly 14 km s $^{-1}$ over the underlying astrophysical distribution width.

To illustrate the impact of the variations in the MaNGA LSF systematic, Fig. 15 displays the distribution of corrected $H\alpha$ linewidths computed in three different ways. We continue to use only

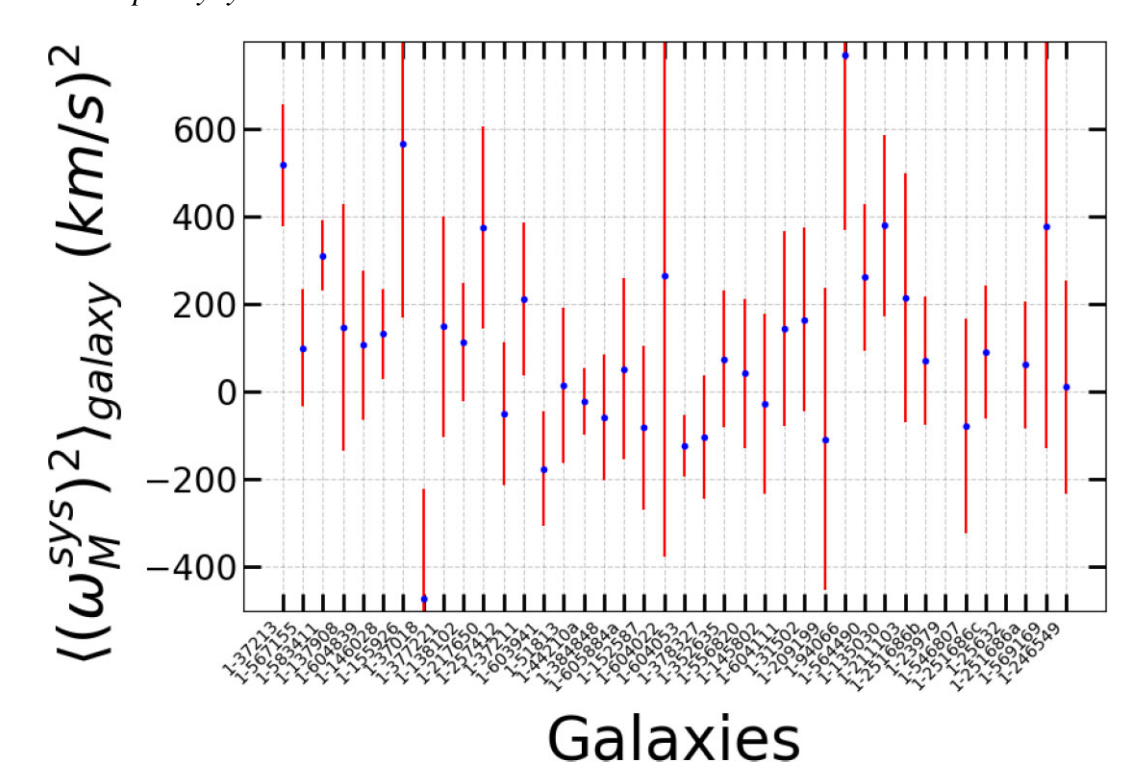


Figure 13. Median of $(\omega_{\rm M}^{\rm sys})^2$ for each galaxy in our sample, denoted $\langle (\omega_{\rm M}^{\rm sys})^2 \rangle_{\rm galaxy}$, computed over all HexPak fibres matched to MaNGA data-cube spaxels that satisfy the conditions that the HexPak SNR > 10, the median MaNGA spaxel SNR > 50 for spaxels in the HexPak fibre footprint, and the HexPak fibre radii are between 4 and 15 arcsec. Error bars represent the standard deviation of $(\omega_{\rm M}^{\rm sys})^2$.

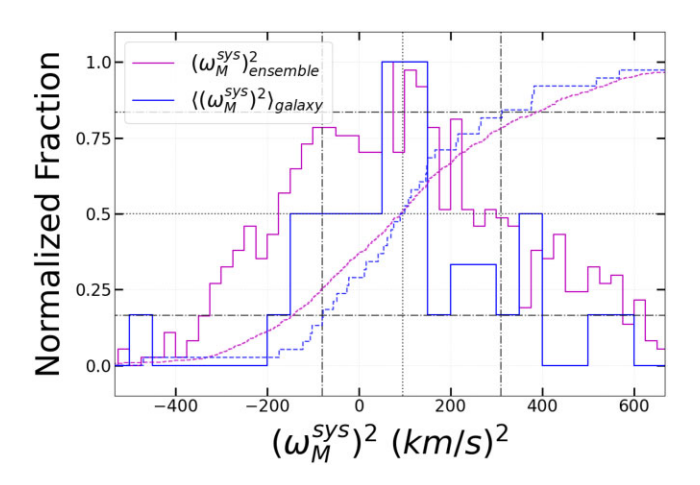
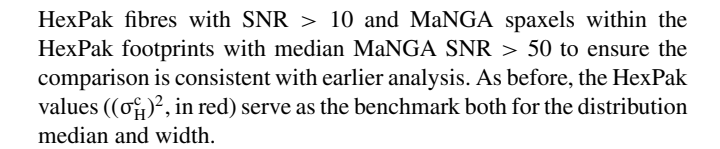


Figure 14. Normalized differential histograms and cumulative distributions (CDF) of $(\omega_{\rm M}^{\rm Sys})^2$ for the median values of each galaxy (blue, $((\omega_{\rm M}^{\rm Sys})^2)_{\rm galaxy}$), and separately for individual measurements in all galaxies for all HexPak fibres and corresponding MaNGA spaxels that meet SNR and radial criteria given in the text (purple, $(\omega_{\rm M}^{\rm Sys})_{\rm seemble}^2$). The 50 per cent of the CDF for both distributions is marked with a black vertical dotted line at a value corresponding to a median $\omega_{\rm M}^{\rm Sys}$ of 9.8 km s⁻¹($(\omega_{\rm M}^{\rm Sys})_{\rm galaxy}^2$ = 96.0 km² s⁻²). The black dash dot vertical and horizontal lines denote the 67 per cent confidence level measured from $(\omega_{\rm M}^{\rm Sys})_{\rm galaxy}^2$ which is found to be 19.7 km s⁻¹.



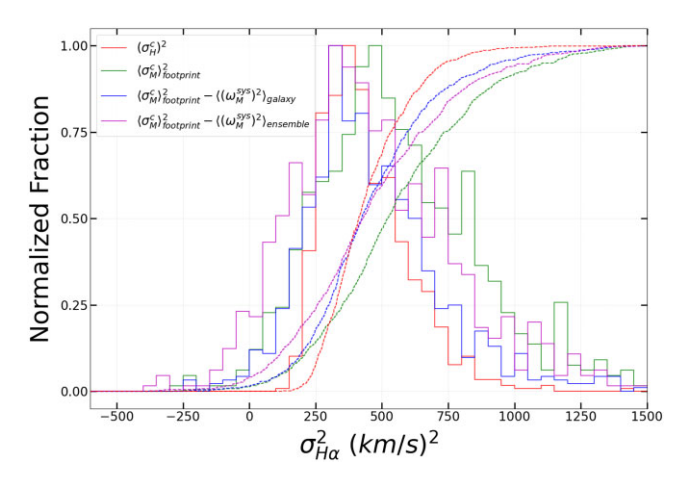


Figure 15. Normalized differential histograms and CDFs comparing the distribution of the LSF-corrected $\sigma_{H\alpha}$ for HexPak and MaNGA data, with and without corrections for systematic errors in the MaNGA LSF. All MaNGA spaxels located within a HexPak footprint (with median MaNGA SNR >50) at radial distance between 4 and 15 arcsec are used. Red curves represent $(\sigma_{\rm H}^c)^2$: the distribution of all LSF-corrected Hexpak fibre measurements with SNR > 10. Green curves represent $\langle(\sigma_{\rm M}^c)^2\rangle$: the distribution of LSF-corrected MaNGA spaxel measurements without any systematic correction to the LSF. Magenta curves represent $\langle(\sigma_{\rm M}^c)^2\rangle - \langle(\omega_{\rm M}^{\rm SyS})^2\rangle_{\rm ensemble}$: the distribution of of MaNGA spaxel measurements with a systematic correction to the MaNGA LSF using the median value of $\langle(\omega_{\rm M}^{\rm SyS})^2\rangle$ for our sample. Blue curve represents $\langle(\sigma_{\rm M}^c)^2\rangle - \langle(\omega_{\rm M}^{\rm SyS})^2\rangle_{\rm galaxy}$: the distribution of of MaNGA spaxel measurements with systematic correction to the MaNGA LSF of respective galaxy using the $\langle(\omega_{\rm M}^{\rm SyS})^2\rangle$ of that galaxy.

(i) First we compare this distribution to the LSF-corrected MaNGA line-width defined by equation (3) ($(\sigma_M^c)^2$, in green) using the nominal LSF values from the DAP, ω_M ; the distribution clearly has both a larger median and width.

We then recompute the LSF-corrected MaNGA line-width to take into account our estimated systematic correction to the MaNGA LSF by substituting $\omega_{\rm M}^{\rm c}$ for $\omega_{\rm M}$ in equation (3). Following equation (4) we can do this in two ways by assigning $(\omega_{\rm M}^{\rm sys})^2$ either (ii) to the median value from Fig. 14, i.e. the same correction for every measurement (purple); or (iii) to $\langle (\omega_{\rm M}^{\rm sys})^2 \rangle_{\rm galaxy}$ for measurements on a galaxy by galaxy basis (blue).

Both of the distributions corrected for the LSF systematic (cases ii and iii) have median values that closely match the HexPak value, which follows from the results of Fig. 14. However, when applying the systematic correction to the MaNGA LSF on a galaxy by galaxy basis (case iii), the width of the distribution narrows and comes into closer agreement with the HexPak distribution width. Indeed, the standard deviation derived from the 67 per cent confidence range, in linear units, decreases from 16.9 to 15.7 km s⁻¹ (case ii to case iii), compared to 12.4 km s⁻¹ for HexPak. The difference in the distribution width between these two cases is comparable to the differences seen in Fig. 14, as would be expected. That the case (iii) distribution remains substantially broader than the HexPak distribution might suggest there remain uncorrected LSF systematic variations with spatial position within each data-cube; as seen in fig. 12 of Law et al. (2021a), LSF spatial variations are present due to the mapping of fibres to different spectrograph slit blocks. With the limited re-calibration offered by this study, the broader distribution represented by the purple curve is what can be expected for the full MaNGA sample SNR > 50.

5.2 Limiting SNR

The results from simulations in Fig. 7 indicate that the median estimator may remain an accurate measure of line-width below the recommended cutoff of SNR = 50 when using the corrected mean formulation from Law et al. (2021a). To test this we can make the astrophysical assumption that if we examine the distribution of line-widths from MaNGA spaxels with H II-like line-ratios, the median width should be independent of SNR. However, the spaxel SNR in the H α line for MaNGA data correlates with the star-formation surface-density (Σ_{SFR}). As Law et al. (2022) and many others have shown, and as we will explore in the following section, there is indeed a correlation between line-width and Σ_{SFR} , whereby line-width increases with Σ_{SFR} . Nonetheless the trend is sufficiently shallow that over a modest range in SNR our assumption of near-constancy in line-width for H II-like spaxels should suffice.

We select MaNGA spaxels in the same way as Law et al. (2022) using these criteria:

- (i) SNR > 3 for H β , [O III], [N II], and [S II],
- (ii) $\sigma_{H\alpha} < 100 \text{ km s}^{-1}$,
- (iii) radii >4 arcsec to avoid beam smearing effects, and
- (iv) line-emission is consistent with star-forming regions defined by Baldwin, Phillips & Terlevich (1981) based on line-ratios [equation (2) from Law et al. (2021b)].

Rather than limiting SNR > 50 as done by Law et al. (2022), we aggregate measurements of line-width, made at the spaxel level, in bins of SNR. Here we use all spaxels within 4–15 arcsec radius for all galaxies in our sample, regardless of whether they fall within a HexPak footprint. We then compute the median and 67 per cent CL of the LSF-corrected line width in each bin, using our systematic

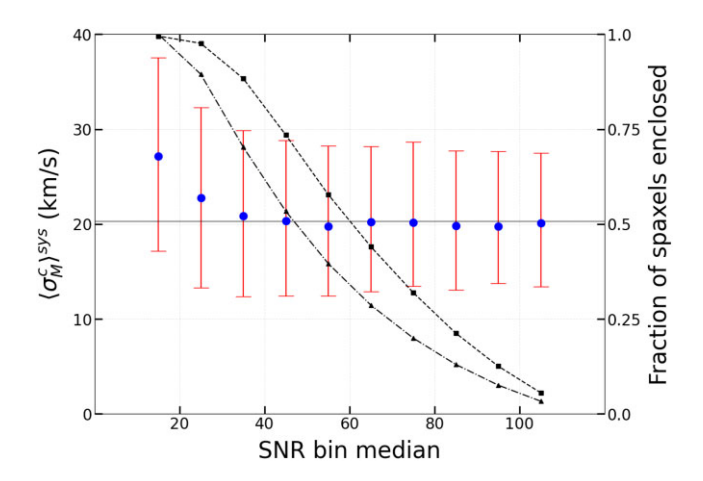


Figure 16. Median and 67 per cent confidence range of the fully corrected MaNGA H α line-widths of all star-froming MaNGA spaxels, $\langle \sigma_n^c \rangle^{sys}$ (equation 7), located between 4 and 15 arcsec radially from the centre, versus spaxel SNR. The solid black line shows the HexPak median for HexPak fibres with SNR > 10. The trend (or lack thereof) in the median points for MaNGA data shows that the SNR threshold of MaNGA spaxels for reliable line-width measurements can be as low as SNR = 30. The dashed and dash—dotted lines represents cumulative number of spaxels included as a function of decreasing SNR for our sample and for all MaNGA star-forming spaxels respectively. A SNR > 50 cutoff includes only 57 per cent of spaxels in our sample while SNR > 30 includes almost 88 per cent of the spaxels. The number of included spaxels are slightly lower at 39 per cent and 70 per cent for the entire MaNGA sample at SNR cutoffs of 50 and 30, respectively.

correction to the MaNGA LSF,

$$\left\langle \sigma_{\rm M}^{\rm c} \right\rangle^{\rm sys} \equiv \sqrt{\left\langle \left(\sigma_{\rm M}^{\rm c}\right)^2 - \left(\omega_{\rm M}^{\rm sys}\right)_{\rm ensemble}^2 \right\rangle}.$$
 (7)

We specifically use $(\omega_{\rm M}^{\rm sys})_{\rm ensemble}$ to understand the behaviour of the corrected line-width as it would be applied to any of the MaNGA data.

Fig. 16 shows the change with SNR in the median values of $\langle \sigma_M^c \rangle^{sys}$ and the uncertainty corresponding to the 67 per cent CL. The flat profile with SNR shows that the median estimator applied to the squared difference of observed line-width and LSF is constant over a factor of \sim 3 in SNR, down to a SNR threshold >30. The upturn at SNR <30 may reflect an astrophysical effect at low Σ_{SFR} , or contamination from a broader-lined, diffuse ionized gas component at low SNR where the culling based on line ratios is more uncertain. By reducing the SNR threshold from 50 to 30, this increases the fraction of all MaNGA spaxels for gas line-width measurements by nearly a factor of two from 39 per cent to 70 per cent.

5.3 Effect on astrophysical measurement: the star-formation rate – dispersion correlation

As previously noted, Law et al. (2022) and references therein have demonstrated that the velocity dispersion of ionized gas and star-formation rate surface-density (Σ_{SFR}) – both using H α – are correlated, albeit with significant scatter. This scatter is likely due to a combination of measurement error, variations in the coupling efficiency of the radiative and mechanical energy from star formation to the gas, and also geometric effects. We are careful to consider the effects of inclination on our line-of-sight measurements of Σ_{SFR} and $\sigma_{H\,\alpha}$ since our sample is comprised of mostly face-on galaxies while the MaNGA sample, and galaxy samples overall often have, a wide range of inclinations.

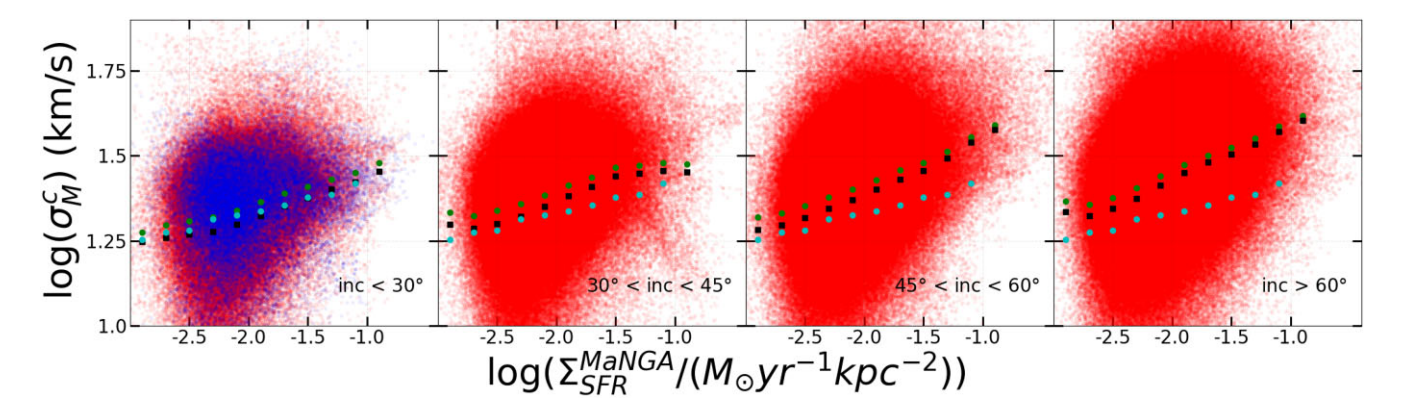


Figure 17. Effect of LSF correction on dispersion – star formation rate surface brightness relation. The red points indicate all MaNGA spaxels after implementing the selection criteria described in the text. The four panels separates the inclination effect. Black and green points are binned mean of all MaNGA spaxels with and without systematic corrections to the MaNGA LSF. The overlaid blue points are MaNGA spaxels of the galaxies in our HexPak sample. The cyan points are the binned mean relation obtained from HexPak observations of our sample of face-on (inc $< 30^{\circ}$) galaxies, repeated in all panels. HexPak and MaNGA binned mean shows impressive agreement in low inclination (left panel, inc $< 30^{\circ}$) and slowly drifts away as the inclination increases demonstrating the effect of inclination in σ - Σ relation.

By virtue of the enormous MaNGA sample of galaxies selected at all inclination and the two dimensional spectral coverage, Law et al. (2022) were able to disentangle some of the geometric effects. In their study a beam-smearing correction is applied to all spaxel measurements to account for the line-of-sight integration through the projected velocity field of an inclined, rotating disc. After making this correction, Law et al. (2022) find evidence for an anisotropic velocity ellipsoid for the ionized gas with the vertical component roughly 10–15 per cent lower than in the in-line components; i.e. the velocity ellipsoid is slightly flattened (and somewhat triaxial).

In our analysis we have not implemented a beam-smearing correction. Both beam-smearing and a flattened velocity ellipsoid will tend to make the projected velocity dispersion larger at higher inclination, while line-of-sight integration will tend to make the projected surface-brightness (Σ) larger by 1/cos (i). These two effects tend to compensate in terms of the $\Sigma-\sigma$ correlation, but also distend the spaxel distribution in this space with increasing inclination.

To illustrate these effects due to inclination, we selected MaNGA spaxels in the same way as given in the previous section with the addition here of SNR > 50 for H α to be fully consistent with Law et al. (2022). We also used the prescription to compute the Σ_{SFR} described equation (2) in Law et al. (2022). We used H α flux and angular distance measured by MaNGA DAP to compute the H α luminosity. We also computed the scale factor representing the solid angled posed by 0.5 arcsec wide MaNGA spaxels. Since we are calculating a surface-density, the quantity is independent of the expansion rate, H_0 . The $H\alpha$ flux provided by the DAP is already corrected for Milky Way extinction, but not for internal extinction from the host galaxy. Hence we corrected the H α luminosity for the latter using the prescription provided by Cardelli, Clayton & Mathis (1989) and the Balmer decrement assuming an intrinsic value of $H\alpha/H\beta = 2.86$. We then applied the systematic correction in σ_M^c to understand the effect of the systematic correction to the MaNGA LSF on the σ versus Σ_{SFR} relation.

Fig. 17 illustrates the effect of our systematic correction to the MaNGA LSF for σ_M^c in galaxies at different inclinations to our line of sight. The red data points denotes LSF corrected dispersion in linear space (i.e. with survival bias) of all MaNGA spaxels within the above itemized criteria, but for different ranges of inclination in each panel. The blue points are MaNGA spaxels from our sample following the same criteria, repeated in all four panels for

comparison; these galaxies are predominantly at low inclination (b/a > 0.7) as evident by the good match to the full MaNGA sample for $i < 30^{\circ}$.

Comparison of HexPak and MaNGA average dispersions in bins of star-formation surface-density in Fig. 17 emphasize the effect of inclination and the systematic correction to the MaNGA LSF: Green circles are $\overline{\sigma_{M}^{c}}$, the 2.5 σ clipped average of all MaNGA data in a given inclination bin. Black squares are $(\overline{\sigma_{M}^{c}})^{sys}$, the same statistics applied after the data are corrected at the spaxel level by $(\langle a_{M}^{sys} \rangle)^{2}$. The cyan circles denotes the binned average of HexPak observations, also LSF corrected, which are repeated in each panel for reference. We computed the HexPak star formation surface brightness (Σ_{SFR}^{HexPak}) via calibrating the HexPak flux against the median Σ_{SFR}^{MaNGA} within individual HexPak footprint using a linear relation. We then use this relation to convert the binned Σ_{SFR}^{MaNGA} to Σ_{SFR}^{HexPak} to locate the cyan points representing the median of σ_{H}^{c} within the same surface brightness interval.

Qualitatively, as expected (1) with larger inclination, the binned average of the MaNGA sample deviates from the HexPak (lowinclination) sample and becomes steeper; (2) the correction factor is more dominant in the lower σ_M^c –lower Σ_{SFR} region, making the relation steeper particularly in the higher inclination bins which is due to the sample selection and not a bias in the MaNGA lSF; and (3) the face-on HexPak sample produces an identical relation to that MaNGA spaxels in galaxies with inclination $<\!30^\circ.$

To quantify these effects, we fit a linear relation between log $\sigma_{H\alpha}$ and log Σ_{SFR}^{MaNGA} for each of $\sigma_{H\alpha}=\overline{\sigma_M^c}, (\overline{\sigma_M^c})^{sys}$, and σ_H^c over the range $-0.2 < \log \Sigma_{SFR}^{MaNGA} < 1.2$ that is well sampled by the MaNGA data,

$$\log \sigma_{\text{H}\alpha} = \log \sigma_{-2.5} + p \times \left[2.5 + \log \left(\Sigma_{\text{SFR}}^{\text{MaNGA}} \right) \right]$$
 (8)

where p describes the power-law index between $\sigma_{\rm H\alpha}$ and $\Sigma_{\rm SFR}^{\rm MaNGA}$, and $\log \sigma_{-2.5}$ (the intercept) is the fitted value of $\log \sigma_{\rm H\alpha}$ at $\Sigma_{\rm SFR}^{\rm MaNGA} = -2.5$. We fit all MaNGA spaxels that follow the above criteria in separate inclination bins. The results are found in Table 1. The fit parameters at low inclination for all measures agree well, with systematic increase in both p and $\log \sigma_{-2.5}$ with inclination. For $i < 30^\circ$, p is identical for $\overline{\sigma_{\rm M}^c}$ and $\overline{(\sigma_{\rm M}^c)^{\rm sys}}$, and slightly steeper than for $\sigma_{\rm H}^c$, but the zeropoint $\sigma_{-2.5}$ for $(\overline{\sigma_{\rm M}^c})^{\rm sys}$ matches to $\sigma_{\rm H}^c$ within 1σ error

Table 1. Power-law model parameters for gas line-width σ and star-formation surface-density $\Sigma_{SFR}.$

	Inclination	p	$\sigma_{-2.5} (\text{km s}^{-1})$		
$\overline{\sigma_{\rm M}^{\rm c}}$	0°-30°	0.11 ± 0.07	20.0 ± 0.95		
	30°–45°	0.13 ± 0.04	20.9 ± 0.57		
	$45^{\circ}-60^{\circ}$	0.13 ± 0.03	22.4 ± 0.42		
	60°–90°	0.16 ± 0.08	23.4 ± 1.27		
$\overline{(\sigma_{M}^{c})^{sys}}$	0 °−30°	0.11 ± 0.1	17.8 ± 1.27		
141	30°–45°	0.14 ± 0.05	20.0 ± 0.65		
	$45^{\circ}-60^{\circ}$	0.14 ± 0.03	20.9 ± 0.46		
	$60^{\circ}-90^{\circ}$	0.17 ± 0.09	22.4 ± 1.52		
σ_{H}^{c}		0.09 ± 0.06	18.6 ± 0.81		

6 CONCLUSIONS

We have measured the systematic error in previous estimates of the MaNGA LSF in the H α wavelength region by directly comparing MaNGA measurements of ionized gas line-widths to independent measurements from high-resolution data taken with the HexPak IFU. Uncertainties in the HexPak instrumental resolution are sufficiently small to allow us to calibrate the MaNGA instrumental resolution to better than 0.1 per cent.

We have also developed an approach to correcting observed linewidths for instrumental broadening by working with the squared differences of observed and instrumental dispersions rather than their square root. This avoids issues with survival bias as well as associated uncertainties for its correction due to modeling the random error distribution. Based on simulations we find that the square root of the median value of the corrected line-width (i.e. squared differences) is an unbiased measure of the median of the astrophysical line-width with <2 per cent systematic error down to SN = 30 at astrohphysically relevant dispersions (a thermal broadening limit of $\sigma=9~{\rm km~s^{-1}})$ regardless of the detailed random error distribution. We refer to this as the squared-median method.

The squared-median method has been applied to a sample of low inclination, star-forming galaxies in a radial region where beamsmearing effects are negligible. For MaNGA spaxels spatially colocated within the larger HexPak fibre footprints where both the HexPak fibre SNR >10 and the median MaNGA spaxel SNR >50, we find the MANGA LSF is underestimated by $\sim\!\!1$ per cent at H α wavelengths on average. This is equivalent to a $\sim\!\!9.8~{\rm km\,s^{-1}}$ correction added in quadrature to the nominal MaNGA LSF of 67.6 km s $^{-1}$, yielding a corrected LSF of 68.3 km s $^{-1}$ at H α wavelengths. This correction is remarkably small, which is testament to the careful calibration in the MaNGA DRP (Law et al. 2016, 2021a).

There remains a real variation in the LSF systematic that varies from galaxy to galaxy and likely within the different spatial elements sampling a single galaxy. This is not surprising given the discrete changes in the MaNGA LSF between integral-field fibre bundles and within fibre bundles that map to different discrete slit-blocks in the BOSS spectrographs (Law et al. 2021a). The re-calibration of the MaNGA LSF here, since it is based on a handful of galaxies, cannot address these variations for the full MaNGA sample. While the systematic correction to the LSF above should yield accurate median corrected astrophysical line-widths, we estimate that any distribution function of astrophysical line-widths is likely broadened by a 14 km s⁻¹ dispersion due to these galaxy-to-galaxy and internal LSF variations.

Application of this systematic correction to the MaNGA instrumental dispersion yields two pertinent results. First, the median corrected (astrophysical) dispersion for H II-like line-emission in our calibrator sample, binned by SNR in the H α line at the spaxel level, is found to be constant at 20 km s^{-1} between 30 < SNR < 110. This suggests that the squared-median method can be applied robustly to a limiting SNR of 30, yielding nearly a factor of two increase in spaxels available for kinematic measurements compared to earlier MaNGA studies limited to SNR > 50. Secondly, we have revisited the correlation between ionized gas velocity dispersion and star-formation surface-density (Σ_{SFR}). Here, we have analyzed the full MaNGA data, limited by SNR > 50 for direct comparison with Law et al. (2022). As expected, there is an inclination dependence to the relation, primarily due to line-of-sight effects on the observed line-width. For the subset of MaNGA galaxies with 0°-30° inclination (comparable to our calibrator sample), we find power-law fits that are comparable for HexPak and MaNGA data. The agreement becomes marginally better when the systematic correction to the MaNGA LSF is applied. This indicates the results from Law et al. (2022) are robust to these small changes in the MaNGA LSF.

Given the small variations in recovered (LSF-corrected) line widths for nebular emission over a broad range in wavelength in MaNGA data (Law et al. 2021a), the mean correction determined here can likely be applied across all wavelengths as a zeropoint shift in the MaNGA LSF vector. Future analysis of high-resolution linewidths measurements for H β and [O III] will verify this and extend the calibration to stellar velocity dispersions.

ACKNOWLEDGEMENTS

MAB acknowledges support from NSF AST-1517006 and AST-1814682. SC and MAB acknowledge support from NRF/SARChI-

Funding for the Sloan Digital Sky Survey IV has been provided by the Alfred P. Sloan Foundation, the U.S. Department of Energy Office of Science, and the Participating Institutions. SDSS-IV acknowledges support and resources from the Center for High-Performance Computing at the University of Utah. The SDSS website is www.sdss.org.

SDSS-IV is managed by the Astrophysical Research Consortium for the Participating Institutions of the SDSS Collaboration including the Brazilian Participation Group, the Carnegie Institution for Science, Carnegie Mellon University, the Chilean Participation Group, the French Participation Group, Harvard-Smithsonian Center for Astrophysics, Instituto de Astrofísica de Canarias, The Johns Hopkins University, Kavli Institute for the Physics and Mathematics of the Universe (IPMU)/University of Tokyo, the Korean Participation Group, Lawrence Berkeley National Laboratory, Leibniz Institut für Astrophysik Potsdam g), Max-Planck-Institut für Astrophysik (MPA Garching), Max-Planck-Institut für Extraterrestrische Physik (MPE), National Astronomical Observatories of China, New Mexico State University, New York University, Uni- versity of Notre Dame, Observatário Nacional/MCTI, The Ohio State University, Pennsylvania State University, Shanghai Astronomical Observatory, United Kingdom Participation Group, Universidad Nacional Autónoma de México, Univer- sity of Arizona, University of Colourado Boulder, University of Oxford, University of Portsmouth, University of Utah, University of Virginia, University of Washington, University of Wisconsin, Vanderbilt University, and Yale University.

DATA AVAILABILITY

The data underlying this article will be shared on reasonable request to the corresponding author.

REFERENCES

Abdurro'uf et al., 2022, ApJS, 259, 35

Aguado D. S. et al., 2019, ApJS, 240, 23

Andersen D. R., Bershady M. A., Sparke L. S., Gallagher J. S. III, Wilcots E. M., van Driel W., Monnier-Ragaigne D., 2006, ApJS, 166, 505

Baldwin J. A., Phillips M. M., Terlevich R., 1981, PASP, 93, 5

Belfiore F. et al., 2016, MNRAS, 461, 3111

Belfiore F. et al., 2019, AJ, 158, 160

Bender R., Burstein D., Faber S. M., 1992, ApJ, 399, 462

Bershady M. A., Andersen D. R., Verheijen M. A. W., Westfall K. B., Crawford S. M., Swaters R. A., 2005, ApJS, 156, 311

Bershady M. et al., 2008, in McLean I. S., Casali M. M., eds, Proc. SPIE Conf. Ser. Vol. 7014, Ground-based and Airborne Instrumentation for Astronomy II. SPIE, Bellingham. p. 70140H

Bershady M. A., Verheijen M. A. W., Swaters R. A., Andersen D. R., Westfall K. B., Martinsson T., 2010a, ApJ, 716, 198

Bershady M. A., Verheijen M. A. W., Westfall K. B., Andersen D. R., Swaters R. A., Martinsson T., 2010b, ApJ, 716, 234

Blanton M. R., Kazin E., Muna D., Weaver B. A., Price-Whelan A., 2011, AJ, 142, 31

Blanton M. R. et al., 2017, AJ, 154, 28

Bundy K. et al., 2015, ApJ, 798, 7

Cappellari M., 2017, MNRAS, 466, 798

Cappellari M., Emsellem E., 2004, PASP, 116, 138

Cardelli J. A., Clayton G. C., Mathis J. S., 1989, ApJ, 345, 245

Drory N. et al., 2015, AJ, 149, 77

Eigenbrot A., Bershady M. A., 2018, ApJ, 853, 114

Epinat B., Amram P., Marcelin M., 2008, MNRAS, 390, 466

Gunn J. E. et al., 2006, AJ, 131, 2332

Knezek P. M. et al., 2010, in McLean I. S., Ramsay S. K., Takami H., eds, Proc. SPIE Conf. Ser. Vol. 7735, Ground-based and Airborne Instrumentation for Astronomy III. SPIE, Bellingham. p. 77357D Law D. R. et al., 2015, AJ, 150, 19

Law D. R. et al., 2016, AJ, 152, 83

Law D. R. et al., 2021a, AJ, 161, 52

Law D. R. et al., 2021b, ApJ, 915, 35

Law D. R. et al., 2022, ApJ, 928, 58

Mackay D. J. C., 2003, Information Theory, Inference and Learning Algorithms, Cambridge University Press, UK

Martinsson T. P. K., Verheijen M. A. W., Westfall K. B., Bershady M. A., Schechtman-Rook A., Andersen D. R., Swaters R. A., 2013, A&A, 557, A130

Melnick J., Terlevich R., Moles M., 1988, MNRAS, 235, 297

Mingozzi M. et al., 2020, A&A, 636, A42

Neumann J. et al., 2022, MNRAS, 513, 5988

Penny S. J., Janz J., Forbes D. A., Benson A. J., Mould J., 2015, MNRAS, 453, 3635

Penny S. J. et al., 2018, MNRAS, 476, 979

Robertson J. G., 2017, PASA, 34, e035

Sánchez S. F. et al., 2022, ApJS, 262, 36

Schaefer A. L., Tremonti C., Belfiore F., Pace Z., Bershady M. A., Andrews B. H., Drory N., 2020, ApJ, 890, L3

Shetty S., Bershady M. A., Westfall K. B., Cappellari M., Drory N., Law D. R., Yan R., Bundy K., 2020, ApJ, 901, 101

Smee S. A. et al., 2013, AJ, 146, 32

Terlevich R., Melnick J., 1981, MNRAS, 195, 839

Wake D. A. et al., 2017, AJ, 154, 86

Westfall K. B., Bershady M. A., Verheijen M. A. W., 2011, ApJS, 193, 21

Westfall K. B., Andersen D. R., Bershady M. A., Martinsson T. P. K., Swaters R. A., Verheijen M. A. W., 2014, ApJ, 785, 43

Westfall K. B. et al., 2019, AJ, 158, 231

Wood C. M. et al., 2012, in McLean I. S., Ramsay S. K., Takami H., eds, Proc. SPIE Conf. Ser. Vol. 8446, Ground-based and Airborne Instrumentation for Astronomy IV. SPIE, Bellingham. p. 84462W

Yan R. et al., 2016a, AJ, 151, 8

Yan R. et al., 2016b, AJ, 152, 197

Yang M., Weijmans A.-M., Bershady M. A., Merrifield M., Boardman N. F., Drory N., 2021, MNRAS, 504, 2658

APPENDIX A: TARGET SAMPLE

Table A1 lists the MaNGA galaxies observed in this HexPak program. The table contains the MaNGA ID (MID), plate and IFU from the MaNGA survey, celestial coordinates, some salient photometric properties, the spectroscopic redshift, and the HexPak run. The Sersic index (n_S), total stellar mass (M*), and absolute magnitudes in g and i bands (adopting $\omega_{\rm m}=0.3$, $\omega_{\Lambda}=0.7$, $H_0=100$ km s⁻¹ Mpc⁻¹), rest-frame NUV-r colour, the half-light radius (r_{05}), and redshift are taken from NASA-Sloan Atlas (NSA; Blanton et al. 2011). Magnitudes are given in the AB system.

Table A1. Galaxy sample.

MID	Plate-IFU	RA (2000) (h:m:s)	DEC (2000) (d:m:s)	n_S	$^{\mathrm{M*}}_{(10^{9}\mathrm{M}_{\odot}h^{-1})}$	$\begin{array}{c} M_i - 5{\log h} \\ \text{(mag)} \end{array}$	$M_g - 5\log h$ (mag)	NUV-r (mag)	r ₀₅ (arcsec)	Z	Run ^c
1-31502a	8656–1901	00:30:52.176	00:31:43.53	1.330	1.289	- 18.351	- 17.816	1.916	6.372	0.019	С
1-37018	8077-12704	02:45:07.336	00:57:00.59	2.678	7.474	- 19.998	-19.229	2.885	9.812	0.025	Α
1–37213	8078-6103	02:49:39.970	-00:04:11.46	1.902	23.87	-21.172	-20.355	3.057	6.417	0.028	A
1-37211	8078-12703	02:50:16.864	00:05:31.16	2.062	29.76	-21.335	-20.480	2.874	10.696	0.028	A
-603941 ^a	8154-9102	03:03:50.459	-00:12:16.04	0.953	12.87	-20.782	-20.173	2.306	8.175	0.028	C
-604022^a	8080-12703	03:17:57.072	-00:10:08.76	1.111	32.46	-21.543	-20.794	2.468	11.072	0.023	C
-583411	8083-12702	03:20:58.900	-00:22:03.66	2.642	29.78	-21.730	-21.023	2.578	28.865	0.021	Α
-604053	8083-12704	03:22:47.228	00:08:57.72	0.986	17.66	-20.982	-20.251	2.282	14.472	0.023	A,C
-38618^{b}	8084-1902	03:30:29.420	-00:29:19.57	2.698	2.270	-18.446	-17.402	4.907	2.231	0.022	A
-604111	9190-12703	03:37:58.867	-06:16:14.30	1.139	22.59	-21.035	-20.151	2.129	15.797	0.022	C
-51813	8727-12702	03:39:34.894	-06:02:19.93	0.682	6.836	-20.078	-19.429	2.639	12.835	0.022	C
-377221	8132-12702	07:23:33.243	41:26:05.66	3.026	36.51	-21.603	-20.771	2.457	17.813	0.028	Α
-378327	8239-6101	07:41:12.977	47:40:17.32	1.270	5.932	-19.786	-19.113	2.619	14.168	0.021	C
-152587^a	8145-12704	07:44:57.444	28:55:39.01	0.821	4.365	-19.772	-19.109	2.125	8.844	0.023	C
-217650	8726-3703	07:47:41.147	22:46:53.78	1.450	11.75	-20.423	-19.632	2.778	4.993	0.028	A
-604839	8146-12701	07:49:05.806	28:37:09.77	0.676	13.97	-20.847	-19.997	2.396	12.353	0.028	A
-145802	8148-9102	07:51:42.169	27:36:26.62	1.794	2.691	-19.563	-19.021	2.131	7.874	0.026	C
-379255^b	8711-1901	07:53:03.975	52:44:35.53	4.694	1.482	-17.915	-16.882	5.122	1.358	0.018	A
-146028	8147-12703	07:54:22.231	27:00:31.70	0.684	1.077	-20.594	-19.935	2.188	8.663	0.027	A
-44210	8714-6101	07:54:51.899	45:49:21.20	0.745	4.439	-19.915	-19.432	1.969	7.304	0.022	C
-230177^{b}	8942-6101	08:19:35.486	26:21:45.59	1.841	1.950	-18.364	-17.371	3.845	6.060	0.020	Α
-556820	10219-12702	08:22:01.425	21:20:34.35	1.191	8.519	-20.003	-19.113	3.145	8.791	0.022	C
-352635^a	10494-12705	08:24:31.862	54:51:14.00	1.687	19.67	-20.945	-20.168	2.895	14.888	0.025	C
-461292	8241-6101	08:28:11.646	17:22:28.77	2.056	0.500	-18.096	-17.747	1.545	5.818	0.021	C
-384848	9494-9102	08:29:44.361	22:25:27.83	1.502	11.55	-20.579	-19.930	2.178	7.167	0.025	C
-567155	8249-12704	09:09:30.604	45:57:08.46	2.087	29.96	-21.340	-20.465	2.889	12.161	0.027	Α
-137908	8249-12703	09:18:14.205	45:39:06.08	1.473	30.47	-21.437	-20.630	2.770	16.087	0.027	A
-155926	8439-12702	09:26:09.434	49:18:36.72	5.325	27.63	-21.202	-20.145	4.695	8.688	0.027	A
-605884	8439-12703	09:28:32.574	50:47:37.04	0.645	14.66	-20.641	-19.689	3.107	11.824	0.025	C
-138102	8252-6102	09:38:13.909	48:23:17.89	1.376	12.73	-20.487	-19.717	2.570	6.603	0.026	Α
-257412	8945-12705	11:37:16.260	45:45:26.64	1.133	6.067	-19.847	-19.222	1.752	11.586	0.025	A
-258315^a	8261-6102	12:10:49.285	44:30:45.37	2.002	9.398	-20.097	-19.257	2.705	5.550	0.023	A
-209199	8485-9102	15:36:26.766	47:51:17.23	2.260	16.08	-20.677	-19.767	2.961	7.931	0.026	В
-211103	8550-6103	16:30:33.285	39:49:50.62	3.676	14.46	-20.510	-19.616	2.996	6.467	0.025	В
-251686	8335-12705	14:27:02.366	39:57:25.96	0.733	16.52	-20.915	-20.177	2.413	13.532	0.025	В
-564490	8604-12704	16:28:39.485	40:07:25.37	1.030	14.10	-20.667	-19.901	2.739	10.620	0.026	В
-135030^a	8603-12704	16:31:34.530	40:33:56.15	2.595	31.90	-21.327	-20.343	3.728	9.510	0.027	В
-94066	8484-1902	16:34:46.011	45:19:27.52	0.941	10.65	-20.579	-19.836	2.826	12.537	0.025	В
-23979	7991–3702	17:12:38.101	57:19:20.72	2.967	8.923	- 19.883	- 18.724	4.832	4.332	0.027	В
-25632	8611-9101	17:22:41.792	59:51:06.72	3.310	14.10	-20.518	-19.587	3.349	7.198	0.027	В
-246549	8597–12703	15:01:33.354	49:06:44.75	2.332	18.66	- 20.916	- 19.957	3.870	10.677	0.026	В
-569169	8602-12701	16:28:11.561	39:49:18.84	5.960	47.52	-21.644	-20.618	4.722	17.457	0.027	В
-546807	7957–12704	17:09:42.583	36:24:53.82		5.955	- 20.388	-19.832	2.230	12.495	0.028	В

^aVPH observations in Mg I region; ^blow-mass AGN host; ^cA = 14–15, 2018 January 18–21, B = 8–9 June 2018, C = 2018 November 30 and December 1–3.

This paper has been typeset from a TEX/LATEX file prepared by the author.